

# Structural basis for the assembly and quinone transport mechanisms of the dimeric photosynthetic RC-LH1 supercomplex

Peng Cao<sup>1,7,8</sup>, Laura Bracun<sup>2,3,8</sup>, Atsushi Yamagata<sup>3,8</sup>, Bern M. Christianson<sup>2</sup>, Tatsuki Negami<sup>4</sup>, Baohua Zou<sup>1,5</sup>, Tohru Terada<sup>4</sup>, Daniel P. Canniffe<sup>2</sup>, Mikako Shirouzu<sup>3</sup>✉, Mei Li<sup>1</sup>✉ & Lu-Ning Liu<sup>2,6</sup>✉

The reaction center (RC) and light-harvesting complex 1 (LH1) form a RC-LH1 core supercomplex that is vital for the primary reactions of photosynthesis in purple phototrophic bacteria. Some species possess the dimeric RC-LH1 complex with a transmembrane polypeptide PufX, representing the largest photosynthetic complex in anoxygenic phototrophs. However, the details of the architecture and assembly mechanism of the RC-LH1 dimer are unclear. Here we report seven cryo-electron microscopy (cryo-EM) structures of RC-LH1 supercomplexes from *Rhodobacter sphaeroides*. Our structures reveal that two PufX polypeptides are positioned in the center of the S-shaped RC-LH1 dimer, interlocking association between the components and mediating RC-LH1 dimerization. Moreover, we identify another transmembrane peptide, designated PufY, which is located between the RC and LH1 subunits near the LH1 opening. PufY binds a quinone molecule and prevents LH1 subunits from completely encircling the RC, creating a channel for quinone/quinol exchange. Genetic mutagenesis, cryo-EM structures, and computational simulations provide a mechanistic understanding of the assembly and electron transport pathways of the RC-LH1 dimer and elucidate the roles of individual components in ensuring the structural and functional integrity of the photosynthetic supercomplex.

<sup>1</sup>National Laboratory of Biomacromolecules, CAS Center for Excellence in Biomacromolecules, Institute of Biophysics, Chinese Academy of Sciences, Beijing 100101, China. <sup>2</sup>Institute of Systems, Molecular and Integrative Biology, University of Liverpool, Liverpool L69 7ZB, UK. <sup>3</sup>Laboratory for Protein Functional and Structural Biology, RIKEN Center for Biosystems Dynamics Research, 1-7-22 Suehiro-cho, Tsurumi-ku, Yokohama, Kanagawa 230-0045, Japan.

<sup>4</sup>Department of Biotechnology, Graduate School of Agricultural and Life Sciences, University of Tokyo, 1-1-1 Yayoi, Bunkyo-ku, Tokyo 113-8657, Japan.

<sup>5</sup>University of Chinese Academy of Sciences, Beijing 100049, China. <sup>6</sup>College of Marine Life Sciences, and Frontiers Science Center for Deep Ocean Multispheres and Earth System, Ocean University of China, Qingdao 266003, China. <sup>7</sup>Present address: Faculty of Environment and Life, Beijing University of Technology, Beijing 100124, China. <sup>8</sup>These authors contributed equally: Peng Cao, Laura Bracun, Atsushi Yamagata. ✉email: [mikako.shirouzu@riken.jp](mailto:mikako.shirouzu@riken.jp); [meili@ibp.ac.cn](mailto:meili@ibp.ac.cn); [luning.liu@liverpool.ac.uk](mailto:luning.liu@liverpool.ac.uk)

Photosynthesis converts solar radiation into chemical energy to power almost all life on Earth<sup>1</sup>. The photosynthetic systems of purple bacteria represent a model for exploring the assembly and function of photosynthetic apparatus. In purple phototrophic bacteria, the early stage of photosynthesis occurs in the reaction center–light-harvesting 1 (RC–LH1) core supercomplexes that are accommodated within the intra-cytoplasmic membranes (termed chromatophores)<sup>1,2</sup>. The RC–LH1 supercomplex comprises an RC surrounded by the LH1 ring that is made of multiple  $\alpha\beta$ -heterodimers<sup>3,4</sup>. LH1 collects photons directly from sunlight or from the peripheral antenna, light-harvesting complex 2 (LH2), and transfers excitation energy to the RC. The subsequent photo-induced charge separation in the RC initiates a cyclic electron flow between the RC and cytochrome *bc*<sub>1</sub> (Cyt *bc*<sub>1</sub>) complex, which ultimately creates proton gradients across the chromatophore membrane to generate ATP<sup>5,6</sup>.

The compositions and architectures of RC–LH1 supercomplexes exhibit a diversity among various bacterial species<sup>2</sup>. Many RC–LH1 complexes occur as monomers, in which the RC is encircled by a closed LH1 ring of 16  $\alpha\beta$ -heterodimers<sup>7–11</sup>, or an open LH1 ring of 15–16  $\alpha\beta$ -polypeptides with a gap formed by specific transmembrane (TM) polypeptides<sup>12–17</sup>. The *Rhodobacter* genus is characterized by the presence of a PufX polypeptide in RC–LH1, which functions as a molecular cross brace to stabilize the monomeric core complex of *Rhodobacter (Rba.) veldkampii*, mediating a large opening in the LH1 ring for quinone/quinol exchange<sup>17</sup>. In contrast, some *Rhodobacter* species, such as *Rba. sphaeroides*, possess dimeric RC–LH1 core structures, representing the largest photosynthetic complex in anoxygenic phototrophs. Previous electron microscopy and X-ray crystallography studies have shown that the *Rba. sphaeroides* RC–LH1 dimer contains two RCs surrounded by an S-shaped LH1 ring with 28 LH1  $\alpha\beta$ -heterodimers plus 2 PufX polypeptides<sup>18–23</sup>. However, detailed information about the modular structures of the dimeric RC–LH1 complexes that mediate their stepwise assembly and electron flow remain uncharacterized.

Here, we report cryo-electron microscopy (cryo-EM) structures of RC–LH1 complexes from the model purple phototrophic bacterium *Rba. sphaeroides* DSM 158 (strain 2.4.1). These high-resolution structures reveal in detail how PufX and an additional TM polypeptide, PufY, are associated with the RC–LH1 complex and how they mediate dimerization, LH1 encirclement, and quinone transport through the RC–LH1 core supercomplex.

## Results and discussion

**Overall structures of the RC–LH1 supercomplexes.** Wild-type (WT) *Rba. sphaeroides* DSM 158 contains both RC–LH1 monomers and dimers (Fig. S1), corroborated by atomic force microscopy (AFM) imaging of isolated photosynthetic membranes<sup>24,25</sup>. The cryo-EM structure of the RC–LH1 monomer (33 polypeptides, 76 cofactors) at 2.79 Å resolution shows that the RC is surrounded by an open LH1 ring of 14  $\alpha\beta$ -subunits, with a large gap (46 Å) formed by a PufX TM polypeptide that has a tilted angle to the membrane plane (Fig. 1a, Figs. S2–S4, Tables S1, S2). The RC comprises the H, L, and M subunits, a bacteriochlorophyll (BChl) *a* dimer as the special pair to act as the primary electron donor, two BChl *a* monomers, two bacteriopheophytins (BPhes), one spheroidene (SPO) carotenoid, and a Fe<sup>2+</sup> ion, similar to the reported crystal structure<sup>26</sup>. The monomeric RC–LH1 structure resembles the architecture of the RC–LH1–PufX monomer from *Rba. veldkampii*<sup>17</sup>, except for a missing LH1 subunit and additional densities (assigned as PufY, see details below) that are located between the RC and LH1, on the opposite side of PufX near the LH1 opening (Fig. S5).

Cryo-EM single-particle analysis determined two distinct classes of RC–LH1 dimers (Class-1 and Class-2) at 2.74 Å and

2.90 Å resolution, respectively (Fig. 1b, c, Figs. S6, S7, Table S1). The dimers of both classes adopt a two-fold symmetry composed of two identical monomers. The structures of the monomers within the RC–LH1 dimers of both classes and the WT RC–LH1 monomer are closely comparable (Fig. S8).

The Class-1 dimer comprises 66 polypeptides and 148 cofactors, with a molecular mass of 558.4 kDa; the long and short dimensions are 206.7 Å and 117.0 Å, respectively (Fig. 1b, Table S2). The LH1 subunits, composed of 28  $\alpha\beta$ -polypeptide pairs, 56 BChls *a* and 50 SPOs, form an S-shaped structure made up of two C-shaped LH1 rings, with two openings of ~30 Å in distance, encircling the two RCs. In addition, two PufX polypeptides are located at the dimerization interface in the center of the RC–LH1 complex, and two PufY polypeptides are located near the two LH1 openings. The two monomers exhibit a tilted angle of 152° measured at the periplasmic face of the complex. The intrinsic bent architecture of the RC–LH1 dimer could create the local membrane curvature, supported by all-atom molecular dynamics (AAMD) simulations (Fig. S9).

Compared with the Class-1 dimer, the Class-2 dimer (66 polypeptides, 152 cofactors) displays a slightly reduced length spanning the dimer (196.5 Å) and a tilted angle of 158° (Fig. 1c, Table S2); rotational and lateral shifts at the monomer–monomer interface were observed (Fig. S10, Movie S1). Consequently, the continuous S-shaped LH1 array fractures in the middle, resulting in two separated C-shaped LH1 rings with a narrower opening (~20 Å) in the LH1 array than that of the Class-1 dimer. Three ubiquinone molecules (Q<sub>A</sub>, Q<sub>B</sub>, Q<sub>3</sub>) were identified in each monomer of the RC–LH1 supercomplexes, tentatively assigned as ubiquinone-10 (UQ-10) according to the HPLC analysis (Figs. S1, S11). In addition, an extra putative UQ-10 (named as Q<sub>Y</sub>) that is strongly associated with PufY was identified in both the Class-2 dimer and WT monomer (Fig. S11).

**Structure of the LH1 ring.** Both N- and C-termini of LH1- $\alpha$  form short helices, which are hydrogen-bonded with LH1- $\beta_{n+1}$  and LH1- $\beta_{n-1}$ , respectively (Fig. S12). LH1- $\alpha_n$  and LH1- $\alpha_{n-1}$  also form hydrogen bonds through Tyr41–Arg53 residues at the periplasmic side. The RC–LH1 interactions within the dimeric and monomeric structures (Fig. S13, Table S3) resemble those identified in the *Rba. veldkampii* RC–LH1–PufX<sup>17</sup>.

A total of 28 BChls *a* and 25 SPOs were resolved in the LH1 ring of each monomer. The LH1  $\alpha\beta$ -heterodimer sandwiches 2 BChls and 2 SPOs, consistent with previous estimation<sup>18,27</sup>, except for the two LH1 pairs close to the gap: LH1-1 lacks one SPO and LH1-14 has no SPO (Figs. S14, S15). The two carotenoids, SPO- $\alpha$  and SPO- $\beta$ , mediate the associations between LH1<sub>*n*</sub> and LH1<sub>*n+1*</sub> and between LH1<sub>*n*</sub> and LH1<sub>*n-1*</sub>, respectively (Fig. S16). SPO- $\alpha$  projects into the TM region between  $\alpha$ - and  $\beta$ -polypeptides and adopts a similar conformation to the carotenoids in the LH1 of other purple bacteria<sup>3,7–9,12–17</sup>. SPO- $\beta$ , which has not been observed in previously reported RC–LH1 structures, is located at the periplasmic layer between LH1- $\beta_n$  and LH1- $\beta_{n+1}$  (Fig. S16). The additional SPO provides a tightly arranged pigment network within the LH1 barrier (Fig. S16), reducing the possibility for traffic of quinones/quinols through the channels between LH1 subunits as proposed for core complexes with closed LH1 rings<sup>7,8,16,17</sup> and emphasizing the necessity of forming an open LH1 ring in the RC–LH1 dimer and monomer.

The 28 BChl molecules in each monomer encircle an open ring at the periplasmic side (Fig. 1). Comparable Mg–Mg distances were found between the BChls in each LH1  $\alpha\beta$ -subunit (9.1–9.4 Å) and of adjacent pairs (~8.5 Å) (Fig. S10). BChls in the Class-1 dimer form a continuous S-shaped array, ensuring that solar energy absorbed by the LH1 BChls in one monomer

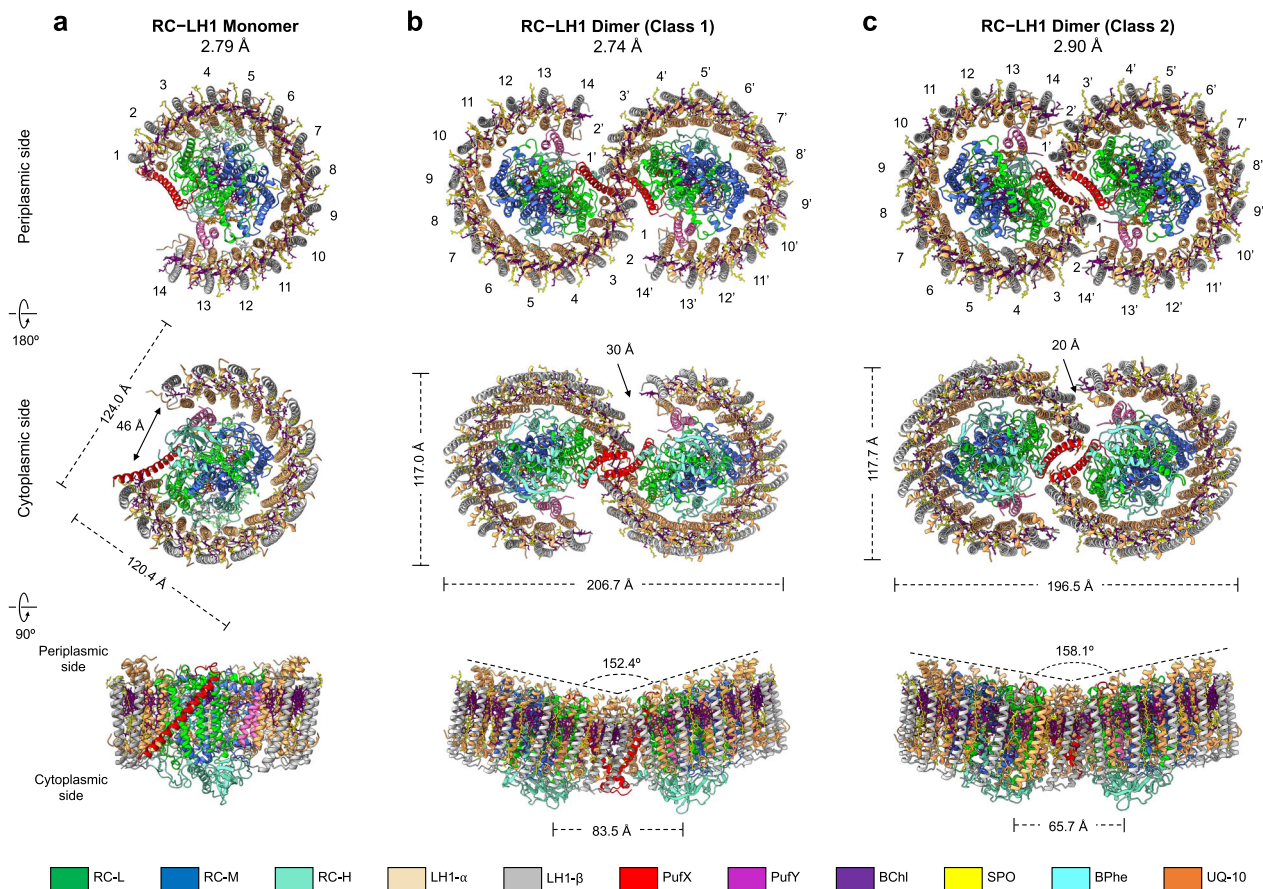


**Fig. 1** Cryo-EM structures of the RC-LH1 core supercomplexes from *Rba. sphaeroides*. **a** The RC-LH1 monomer. Top, view from the periplasmic side; middle, view from the cytoplasmic side; bottom, side view in the membrane plane (facing the PufX-mediated gap region). **b** The Class-1 RC-LH1 dimer. Top, view from the periplasmic side; middle, a view from the cytoplasmic side; bottom, side view in the membrane plane. **c** The Class-2 RC-LH1 dimer. Top, a view from the periplasmic side; middle, view from the cytoplasmic side; bottom, side view in the membrane plane. Color scheme is presented at the bottom as follows: LH1- $\alpha$ , wheat; LH1- $\beta$ , gray; PufX, red; PufY, magenta; RC-L, green; RC-M, marine; RC-H, teal; bacteriochlorophylls (BChls), purple; bacteriopheophytins (BPhe), cyan; carotenoids, yellow; quinones, orange.

can be transferred to the LH1 of the neighboring monomer. This arrangement may provide the foundation for equilibrated, efficient exciton coupling and energy trapping<sup>28</sup>. In contrast, the continuity of the array of excitonically coupled BChls is interrupted at the monomer–monomer interface in the Class-2 dimer, resulting in a ~23-Å gap between adjacent BChls from the two monomers (Figs. S10, S11).

**Location of PufX and its interactions within the RC-LH1 dimer.** PufX (82 amino acids) has been proposed to play roles in dimerization of RC-LH1 and exchange of quinones/quinols between the RC and Cyt  $bc_1$ <sup>22,23,29,30</sup>. However, its precise structure and location within the RC-LH1 dimer have remained elusive. Our cryo-EM structures reveal that two PufX polypeptides are positioned at the dimerization interface of the RC-LH1 supercomplex (Fig. 2), in agreement with AFM and low-resolution EM structures<sup>23,31,32</sup> but distinct from the model inferred from an 8-Å crystal structure (PDB ID: 4V9G), which proposed that PufX is positioned in the gap next to the terminal LH1 subunit and adjacent to the  $Q_B$  site of the RC<sup>18</sup>. The N-terminus of PufX is exposed on the cytoplasmic side of the complex and its C-terminal domain is situated on the periplasmic surface (Fig. 2a, b). The PufX peptide is tilted ~45° from the RC to the peripheral side of LH1 and adopts a slightly bent configuration in the Ala24–Gly36 region within the membrane layer,

resembling the PufX structure from *Rba. veldkampii*<sup>17</sup> (Fig. S17). The crossing angle for the PufX dimer is ~73° (Fig. 2b).

The N-terminal region of PufX (Ala2–Pro15) is well resolved in the Class-1 dimeric structure, revealing that residues Ile6–Asp9 interact with LH1-1 $\alpha\beta$  of the other monomer via hydrogen bonds and salt bridges (Fig. 2c, Table S4). The N-terminal domain of the TM helix of PufX (Thr17–Lys29) forms hydrogen bonds with both RC-H subunits of the dimer at the cytoplasmic side. The N-termini of the two PufX polypeptides are in close proximity to each other at the monomer–monomer interface, albeit without detectable interactions. It is likely that water molecules, which were not identified at the present resolution, mediate PufX–PufX interactions at the N-terminal region. In contrast, the N-terminal domain of PufX (Ala2–Pro15) is not resolved in the structures of the monomer and Class-2 dimer (Fig. S8), presumably due to its disordered structure when not binding with RC-H and LH1-1 subunits of the neighboring monomer. In Class-2, differences in the RC-LH1 association occur at the dimerization interface, and the two N-terminal heads of PufX are further separated, due to the twist of two RC-LH1 monomers, compared with those in Class-1 (Figs. S18, S19).

At the periplasmic side, the C-terminal regions of the two PufX polypeptides are separated by LH1-1 from each monomer and have no close contacts with each other (Fig. 2d). The Arg49–Ala62 residues interact with RC-L (Val137–Tyr144) within the same monomer and LH1-1 $\beta$  of the neighboring monomer through

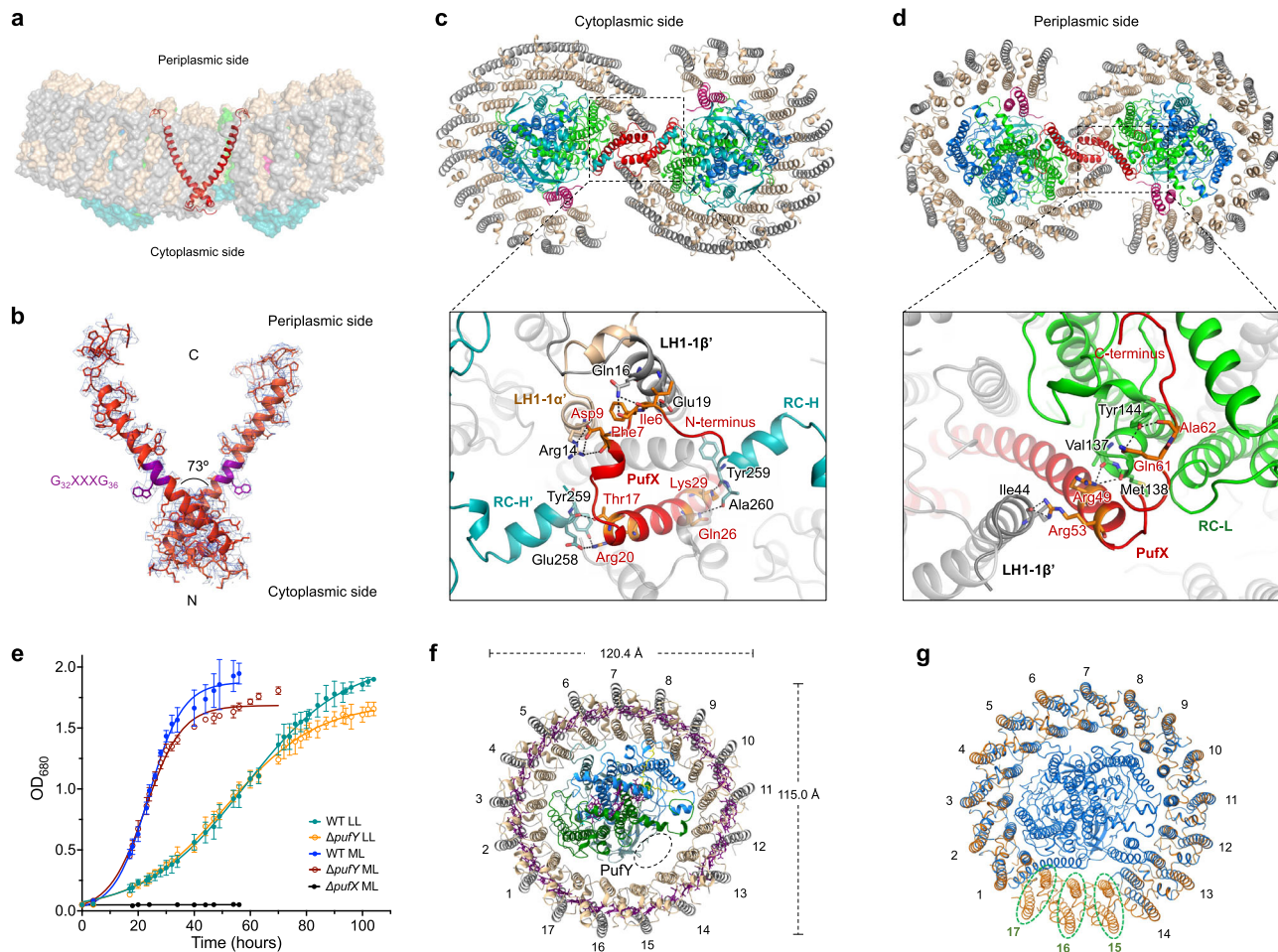


**Fig. 2** The location of PufX and interactions within the RC-LH1 dimer. **a** Two PufX polypeptides (red cartoon) are positioned at the monomer-monomer interface of the RC-LH1 dimer. **b** Cryo-EM densities of the PufX dimer. The  $G_{32}XXXG_{36}$  motif (purple) within the TM helix of PufX, which was assumed to drive TM helix-helix association<sup>89</sup>, does not feature the dimerization interface, and thus does not possibly mediate PufX-PufX dimerization. **c** Interactions between PufX and RC-LH1 subunits at the cytoplasmic side. The residues of PufX, RC-H, LH1-1 $\alpha$ , and LH1-1 $\beta$  involved in the inter-subunit interactions are shown in sticks and colored in orange, teal, wheat, and gray, respectively. All the interacting residues involved in the association between PufX and RC-L are listed in Table S4. **d** Interactions between PufX and RC-LH1 subunits at the periplasmic side. The residues of PufX, RC-L, and LH1-1 $\beta$  involved in the inter-subunit interactions are shown in sticks and colored in orange, green, and gray, respectively. **e** Phototrophic growth of the *Rba. sphaeroides* wild-type (WT),  $\Delta pufX$ , and  $\Delta pufY$  mutants under low light (LL) and moderate light (ML), monitored at  $OD_{680}$  and fitted with logistic growth. The growth rate is  $0.16\text{ h}^{-1}$  for WT and  $0.15\text{ h}^{-1}$  for  $\Delta pufY$  under ML, and  $0.06\text{ h}^{-1}$  for WT and  $\Delta pufY$  under LL. Data are presented as mean values  $\pm$  SD.  $n = 3$  biologically independent cultures. Source data are provided as a Source data file. **f** Cartoon representation of the  $\Delta pufX$  RC-LH1 complex. Without PufX, LH1 forms a complete circle of 17 subunits, surrounding the RC. Mass spectrometry confirmed the presence of PufY in the  $\Delta pufX$  RC-LH1 monomer but PufY exhibits weak densities in the  $\Delta pufX$  RC-LH1 structure. The potential location of PufY is indicated by a dashed circle. **g** Comparison of the structures of the  $\Delta pufX$  RC-LH1<sub>17</sub> monomer (light orange) and the wild-type RC-LH1<sub>14</sub> monomer (blue) from *Rba. sphaeroides*. To highlight the differences in the LH1 architectures, the RC subunits of  $\Delta pufX$  RC-LH1<sub>17</sub> were not shown. The three extra LH1 subunits within the  $\Delta pufX$  RC-LH1<sub>17</sub> monomer are circled.

hydrogen bonds. Due to steric hindrance provided by PufX within the same monomer, and interactions with the PufX of the adjacent monomer, LH1-1 $\alpha$  displays a conformational shift compared with the other LH1 subunits and lacks SPO- $\beta$ ; moreover, both SPO- $\alpha$  and the phytol tail of BChl- $\alpha$  kink at the periplasmic side to interact with PufX (Fig. S14). All these interactions formed by the N- and C-termini of PufX and LH1 interlock the RC-LH1 structures and mediate dimerization of RC-LH1, providing the structural evidence for previous observations<sup>33–36</sup>.

To verify the roles of PufX in the RC-LH1 dimer, we genetically deleted the *pufX* gene (RSP\_0255), which resulted in the exclusive formation of RC-LH1 monomers and loss of capability to perform photoheterotrophic growth (Fig. 2e, Fig. S1), consistent with previous results<sup>34,37–39</sup>. The cryo-EM structure of the  $\Delta pufX$  RC-LH1 monomer at 4.20-Å resolution shows that the

central RC is surrounded by a completely closed LH1 ring of 17 subunits, adopting a slightly elliptical shape ( $120\text{ \AA} \times 115\text{ \AA}$ ) (Fig. 2f, g, Figs. S20, S21, Table S1). The cryo-EM structure explains the previous observation that the absence of PufX resulted in an increase in the ratio of LH1 to RC<sup>40</sup>. The closed LH1 ring and the tightly packed pigments within LH1s impede quinone/quinol exchange, thereby causing the incapability of this mutant strain to grow photosynthetically. We could not obtain a higher-resolution cryo-EM structure of the  $\Delta pufX$  RC-LH1<sub>17</sub> monomer, and the RC and PufY exhibit weaker densities than the peripheral LH1. Mass spectrometry confirmed that  $\sim 27\%$  of PufY was retained in the  $\Delta pufX$  RC-LH1 monomer compared to the WT monomer. The lack of intensive interactions between PufX and the RC-LH1 subunits, which may confine the orientation of the RC inside the LH1 ring<sup>13</sup> and stabilize the association between RC, PufY, and LH1, could result in an unstable assembly

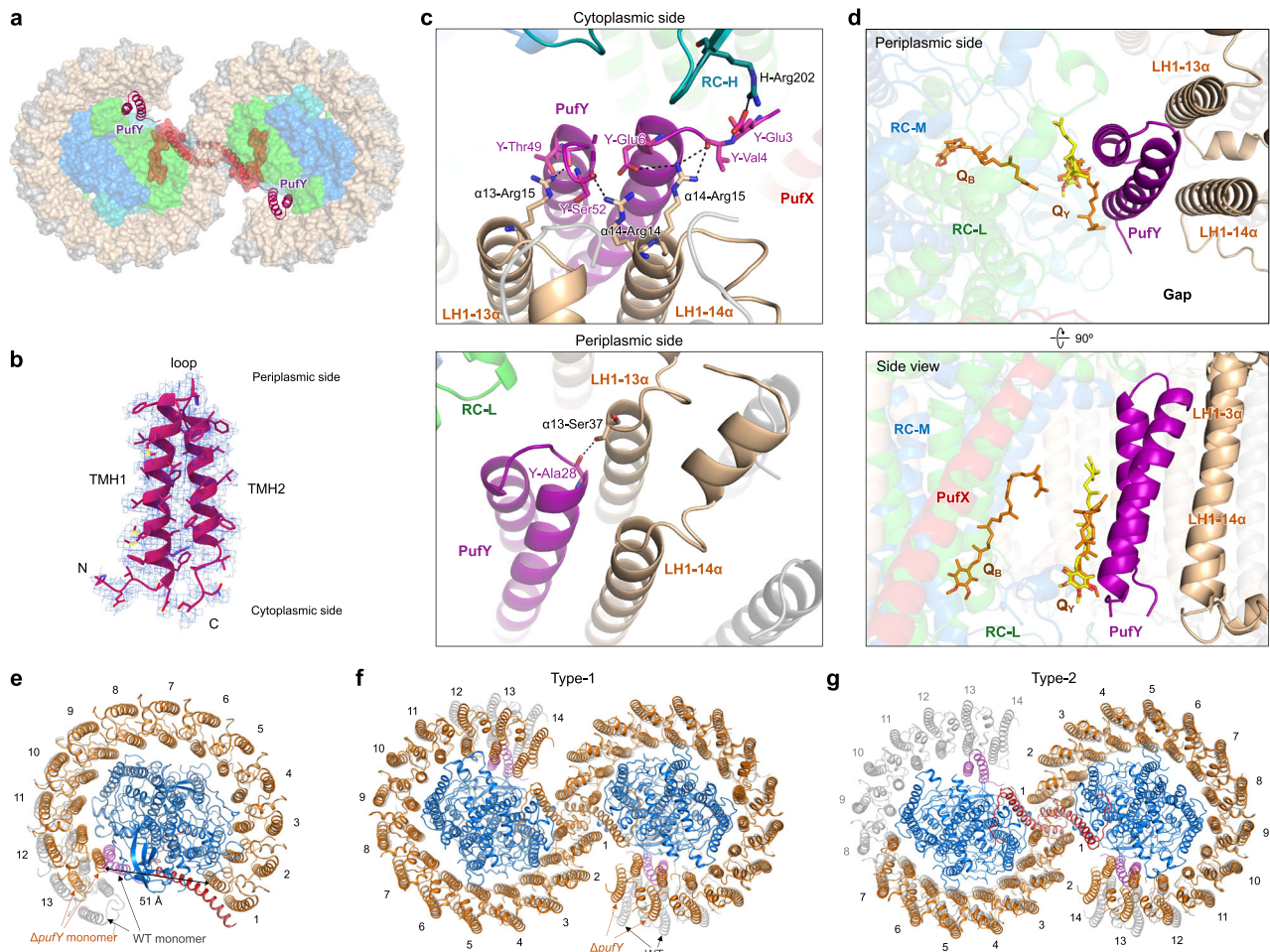


**Fig. 3 The PufY location and interactions within the RC-LH1 dimer.** **a** Two PufY polypeptides (purple cartoon) are positioned between the RC and LH1, close to the gaps of the RC-LH1 dimer (periplasmic view). **b** Cryo-EM density of PufY. **c** Interactions between PufY and RC-LH1 subunits. All the interacting residues involved in the association between PufY and RC-LH1 are listed in Table S5. **d** A quinone molecule ( $Q_Y$ ) is identified in the structures of the Class-2 dimer (yellow) and wild-type monomer (orange), which binds with PufY near the RC  $Q_B$  site. **e** Cryo-EM structure of the  $\Delta pufY$  RC-LH1 monomer (cytoplasmic view, LH1 shown in orange cartoon) shows 13 LH1 subunits surrounding the RC, interlocked by PufX. Comparison with the wild-type RC-LH1<sub>4</sub> monomer (LH1 shown in gray cartoon, PufY in purple cartoon) shows that lack of PufY induces the shift of terminal LH1 subunits towards the RC, and missing of the 14th LH1 subunit creates a larger opening in the LH1 ring of the  $\Delta pufY$  RC-LH1 monomer. **f** Cryo-EM structure of the Type-1  $\Delta pufY$  RC-LH1 dimer (periplasmic view, LH1 shown in orange cartoon) shows a two-fold symmetric dimer with 13–14 LH1 subunits per monomer (the last pair exhibits poor density). Comparison with the wild-type Class-1 RC-LH1 dimer (LH1 shown in gray cartoon, PufY in purple cartoon) shows that lack of PufY induces the shift of terminal LH1 subunits towards the RC and eventually an elliptical shape of the LH1 rings within the  $\Delta pufY$  RC-LH1 dimer. **g** Cryo-EM structure of the Type-2  $\Delta pufY$  RC-LH1 dimer (periplasmic view, LH1 shown in orange cartoon) shows an asymmetric dimer with 13–14 LH1 subunits in one monomer and a partial LH1 ring (only 7–9 LH1 subunits, the last several pairs exhibit poor density) in the other monomer. The structure shows a wide opening in the LH1 ring, compared with the structure of the wild-type Class-1 RC-LH1 dimer (LH1 shown in gray cartoon, PufY in purple cartoon). Note: LH1-9 pair still shows density but is considerably weak, thus was not modeled in the structure.

of RC-LH1 complexes and formation of LH1-only rings, as suggested previously<sup>38,41</sup>.

**Transmembrane polypeptide PufY.** Another distinctive feature of the *Rba. sphaeroides* RC-LH1 structures is the presence of extra densities at the interface between the RC and LH1-13 and LH1-14 subunits, adjacent to the RC  $Q_B$  site (Fig. 3a). This position is close to the location of the previously assigned PufX polypeptide in the low-resolution crystal and cryo-EM structures<sup>18,20</sup>. We identified this protein as RSP\_7571 (termed PufY, equivalent to the Protein-U<sup>42</sup> or Protein-Y<sup>43</sup> reported recently), based on the perfect match of its sequence with the cryo-EM density map (Fig. 3b, Fig. S4) and mass spectrometry results (Fig. S22, Data S1). PufY comprises 53 residues with two parallel TM helices connected by a short loop (Fig. 3b, Fig. S22).

It has a molecular mass of 5553 Da and migrates at the same position as LH1- $\beta$  (5588 Da) in SDS-PAGE (Fig. S1), explaining why it has not been identified in previous studies. Unlike *pufX*, the RSP\_7571 gene encoding PufY is not in proximity to the photosynthesis gene clusters (Fig. S22). Bioinformatic analysis revealed both the protein sequence of PufY and genomic location are highly conserved in all *Rba. sphaeroides* subspecies and several additional *Rhodobacter* species (Fig. S22).

The integration of PufY creates extra space between LH1-13/14 and the RC, compared with the RC-LH1 structures from *Rba. veldkampii*<sup>17</sup> and *Rhodospseudomonas (Rps.) palustris*<sup>13</sup> (Fig. 3a, Fig. S23). Both N- and C-termini of PufY at the cytoplasmic side of the RC-LH1 complex form multiple hydrogen bonds (Glu3-Glu6, Thy49-Ser52) with RC-H (Arg202) and the N-terminal residues (Arg14, Arg15) of LH1-13 $\alpha$  and LH1-14 $\alpha$ . At the periplasmic side, Ala28 at the short loop of PufY is hydrogen-

bonded with Ser37 of LH1-13 $\alpha$  (Fig. 3c, Table S5). Moreover, a putative UQ-10 ( $Q_Y$ ) that associates with PufY and is close to the RC  $Q_B$  site was identified in the cryo-EM maps of the Class-2 dimer and WT monomer, whereas it was not visible in the Class-1 dimer (Fig. 3d). The head group of  $Q_Y$  is located near the cytoplasmic side and is sandwiched by the aromatic rings of RC-M Trp41 and PufY Phe7 via  $\pi$ - $\pi$  interactions, forming a quinone-binding pocket (Fig. S11).

The unique location of PufY and its interactions with the terminal pairs of LH1 and the RC suggest the possible roles of PufY in forming the opening in the LH1 ring and facilitating quinone exchange. Genetic deletion of the *pufY* gene had no notable effect on the oligomerization states of the RC-LH1 complexes (Fig. S1), suggesting that PufY, which is not involved in monomer-monomer interactions, is not essential for dimerization of RC-LH1. Compared to the WT, the  $\Delta pufY$  strain shows a comparable growth rate but a slightly early onset of the stationary phase under both moderate light (ML, 25  $\mu\text{mol photons s}^{-1} \text{m}^{-2}$ ) and low light (LL, 5  $\mu\text{mol photons s}^{-1} \text{m}^{-2}$ ) (Fig. 2e). The cryo-EM structure of the  $\Delta pufY$  RC-LH1 monomer (2.86-Å resolution) shows that the RC is encircled by an LH1 ring of 13 subunits, forming an incomplete RC-LH1 complex with an enlarged LH1 opening of 51 Å adjacent to the  $Q_B$  site (Fig. 3e, Figs. S24, S25). Cryo-EM analysis reveals two classes of the  $\Delta pufY$  RC-LH1 dimers, both possessing an S-shaped LH1 ring (Fig. 3f, g, Figs. S26–29). The Type-1 dimer (3.08-Å resolution) contains 13–14 LH1 subunits in each monomer (Fig. 3f, the last pair exhibits poor densities). The Type-2 dimer (3.45-Å resolution) adopts an asymmetric structure, with one monomer consisting of 13–14 LH1 subunits and the other showing a widely opened LH1 barrier with only 7–9 pairs of LH1  $\alpha\beta$ -polypeptides (the last several pairs exhibit poor densities), completely exposing the RC  $Q_B$  site (Fig. 3g). In the absence of PufY, LH1-12, LH1-13, and LH1-14 shift inward to the RC and follow the contour of the RC, forming a relatively closed, elliptical LH1 ring compared with the monomers of the WT Class-1 dimer (Fig. S30). These results suggest that although PufY does not appear to be essential in maintaining the RC-LH1 functionality like PufX (at least under the tested ML and LL conditions), it stabilizes LH1 and prevents closure of the LH1 ring, thereby facilitating quinone transport to the RC  $Q_B$  site. It may further intimate the importance of dimerization and modularity of the RC-LH1 complex: when the access of quinones to one of the RC  $Q_B$  sites is obstructed, the other RC-LH1 monomer with an incomplete LH1 barrier within the dimer could ensure sufficient quinone/quinol exchange of the whole dimeric complex.

**Assembly pathway of the RC-LH1 dimer.** The cryo-EM structures provide evidence for the stepwise assembly of the dimeric RC-LH1 complex (Fig. 4). PufX interacts with RC-L, RC-H, and the 1st LH1  $\alpha\beta$ -heterodimer within the same RC-LH1 monomer (Fig. 2), suggesting that PufX appears at the early stage of the RC-LH1 assembly, which is supported by biochemical results<sup>35,44</sup>. The association of PufX with the RC provides an anchoring point for the 1st LH1 subunit, initiating the sequential assembly of the LH1 ring around the RC and stabilizing the RC-LH1 association. Incorporation of PufY then leads to recruitment and repositioning of the LH1 terminal subunits near the  $Q_B$  site of the RC, creating a wide channel for efficient quinone/quinol exchange between the RC and Cyt *bc*<sub>1</sub>.

The WT RC-LH1 monomer has a higher structural similarity with the Class-2 dimer than Class-1: The N-terminus of PufX in the WT monomer and Class-2 dimer is subject to conformational flexibility without interactions with the neighboring monomer; no interaction between PufX and RC-H is identified in the WT monomer and

within the same monomer of the Class-2 dimer (Fig. 2, Figs. S8, S18). These results, together with the distinct BChl arrangements (Figs. S10, S11), suggest that the Class-2 dimer may serve as an intermediate structure in the formation of a mature RC-LH1 dimer from monomers. Hence, dimerization of the RC-LH1 core complex may occur after the formation of a complete RC-LH1-PufX-PufY monomer. Two RC-LH1-PufX-PufY monomers associate through the interactions between PufX, RC-H, and LH1-1, forming the Class-2 RC-LH1-PufX-PufY dimer as an intermediate structure. In the final step, the two monomers in the Class-2 dimer twist, driven by increasing inter-monomer interactions, leading to the eventual formation of the Class-1 RC-LH1-PufX-PufY dimer. This hierarchical assembly process signifies the necessity of a modular organization and a flexible dimerization interface of the RC-LH1 core complex. Consistent with this, some monomers and irregular structures are always seen together with dimers in chromatophores<sup>24,45</sup>.

Recently, four polypeptides, termed protein-Z, have been identified in a dimeric RC-LH1 structure from a *Rba. sphaeroides*  $\Delta\text{LH2}$  mutant strain grown under semi-aerobic conditions in darkness<sup>46</sup>. In our Class-1 and Class-2 dimer structures from the *Rba. sphaeroides* WT (DSM 158) strain that was grown phototrophically under anoxic conditions, the cryo-EM densities at the corresponding positions of protein-Z are too weak to determine their presence and organization (Fig. S31), albeit a high global resolution (2.74 Å for Class-1) and local resolution (Fig. S6). This discrepancy is presumably attributed to the distinctive strain growth conditions.

#### Pathways for quinone/quinol exchange in the RC-LH1 dimer.

In the Class-1 dimer, three UQ-10 molecules were identified in each monomer (Fig. 5, Fig. S11). Two are located at the  $Q_A$  and  $Q_B$  sites. The third one (termed  $Q_3$ ) is located near the periplasmic side and its head group projects towards the isoprenoid tail of  $Q_B$ , suggesting its involvement in the exchange of  $Q_B$ . In addition, an extra UQ-10 molecule ( $Q_Y$ ) was identified in the Class-2 dimer and WT monomer at the gap region between PufY and the RC (Figs. 3d, 5), suggesting that PufY might be involved in congregating quinones close to the  $Q_B$  site where quinones are photoreduced and protonated to quinols. The tail of  $Q_Y$  projects into the membrane and is adjacent to the head group of  $Q_3$  and the tail of  $Q_B$ . The three UQ-10 molecules are clustered together, with head-head distances of  $\sim 23$  Å ( $Q_B$ - $Q_3$ ),  $\sim 22$  Å ( $Q_B$ - $Q_Y$ ), and  $\sim 25$  Å ( $Q_3$ - $Q_Y$ ), delineating the routes for quinone/quinol entering or leaving the  $Q_B$  site. Coarse-grained molecular dynamics (CGMD) simulations indicate that  $Q_Y$  could move toward  $Q_3$ , while the  $Q_3$  molecule shifts toward the  $Q_B$  site (Fig. S32, Movies S2, S3), reminiscent of the diving of quinones in membranes<sup>6</sup>.  $Q_Y$  was not identified in the cryo-EM structure of Class-1 dimer, likely due to its high dynamics and transient binding with PufY in the photosynthetically active RC-LH1 dimer (Fig. S32).

The *Rba. sphaeroides* LH1 unit contains two carotenoids, distinct from other reported RC-LH1 complexes that have only one carotenoid per LH1 unit. The tightly arranged pigments within the LH1 array may block the channels between adjacent LH1 subunits for quinone/quinol passage (Fig. S15), consistent with previous results that photosynthetic growth was partially recovered when LH1 was deleted<sup>40</sup> or by decreasing the carotenoid content in the LH1 barrier<sup>27</sup>. In contrast, cryo-EM structures and UQ-10-binding CGMD simulations indicate that the large openings in the S-shaped LH1 ring, formed by PufX and PufY, provide the dominant channels for quinol/quinone exchange of the RC  $Q_B$  site (Fig. 5, Fig. S32, Movie S4). The tilted conformation of PufX and its binding with the RC and LH1 subunits ensure an open LH1 ring. Removal of PufX resulted

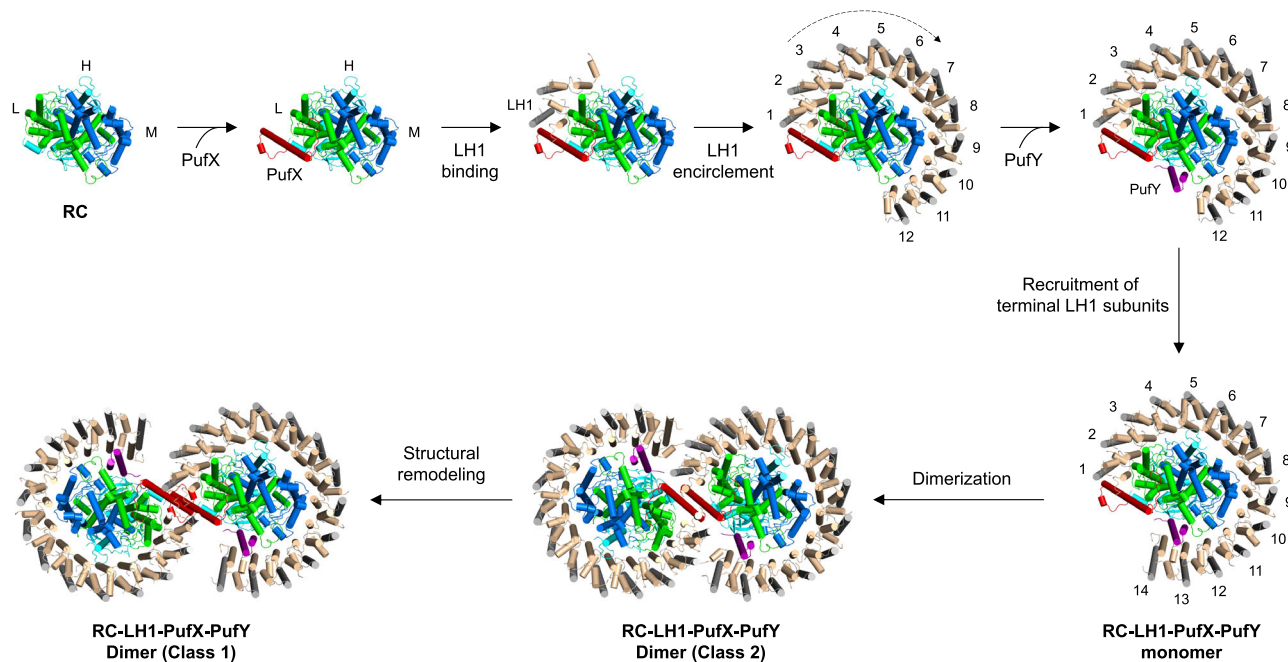


**Fig. 4 A proposed assembly pathway of the dimeric RC-LH1-PufX-PufY core complex.** The sequential assembly of the RC-LH1 dimer starts from the binding of PufX to the RC complex, which provides an anchoring point for binding with the first LH1  $\alpha\beta$ -subunits. This triggers the sequential assembly of LH1 subunits to ensure encirclement of the RC. Association of PufY prevents complete closure of the LH1 ring and creates extra space around the RC  $Q_B$  site to facilitate quinone/quinol binding and diffusion. This eventually generates the RC-LH1-PufX-PufY monomer. Subsequently, the interface of the monomer formed by PufX, RC-H, and LH1 subunits promotes dimerization, resulting in the formation of the Class-2 RC-LH1-PufX-PufY dimer as an intermediate structure. Extensive interactions formed at the monomer-monomer interface eventually create the stable and photosynthetically active Class-1 RC-LH1-PufX-PufY dimer.

in an RC-LH1<sub>17</sub> complex with a completely closed LH1 ring, and thereby the loss of phototrophic viability (Fig. 2). Spectroscopic analysis confirmed that PufX could facilitate the quinone-mediated redox interaction between the RC and Cyt *bc*<sub>1</sub> in *Rba. veldkampii* and *Rba. sphaeroides*<sup>47</sup>. PufY interacts with the terminal LH1 subunits and provides steric hindrances to create additional space near the  $Q_B$  site. The opening adopts a similar location within the LH1 ring as the gaps with varying sizes observed in other reported RC-LH1 structures<sup>7-9,12-14,17</sup> (Fig. S23), implying the general mechanism of quinone transport to/from the  $Q_B$  site.

In summary, our cryo-EM structures describe in detail the hierarchical assembly of the dimeric photosynthetic RC-LH1-PufX-PufY supercomplex and the roles of PufY and PufX in mediating LH1 encirclement and dimerization of the core complex to facilitate rapid shuttle of quinones/quinols between the RC and Cyt *bc*<sub>1</sub>. Our results provide insights into the structural variability and modularity of bacterial photosynthetic complexes, which enable efficient light harvesting, excitation energy transfer, and electron transport that underpin photosynthesis in phototrophic bacteria grown in changing environmental conditions.

## Methods

**Strains, mutagenesis, and growth methods.** *Rba. sphaeroides* wild-type (DSM 158, NCBI:txid272943) and the  $\Delta$ *pufY* mutant were grown phototrophically under anoxic conditions in liquid M22 + medium supplemented with vitamins (0.08 M nicotinic acid, 0.01 M thiamine, 7.3 mM 4-aminobenzoic acid, 0.4 mM d-biotin) and 0.1% casamino acids, at 29 °C in sealed glass bottles under a light intensity of 25  $\mu$ mol photons  $s^{-1} m^{-2}$  provided by Bellingh 70 W halogen bulbs unless specified otherwise. Growth assays of the WT and  $\Delta$ *pufY* strains were performed under low light (LL, 5  $\mu$ mol photons  $s^{-1} m^{-2}$ ) and moderate light (ML, 25  $\mu$ mol photons  $s^{-1} m^{-2}$ ). The non-phototrophic *Rba. sphaeroides*  $\Delta$ *pufX* mutant was grown at 29 °C in the dark in the same medium under microoxic conditions in an orbital shaker set at 150 rpm.

Unmarked genomic deletions were constructed in WT *Rba. sphaeroides* using the allelic exchange suicide vector *pk18mobsacB*<sup>48</sup>. Deletion of *pufX* (RSP\_0255, [<https://www.ncbi.nlm.nih.gov/gene/3719397>]) was conducted as follows: primer pairs XupF and XupR (AGTCTCTAGAGCACCTATCTCCGCGCTCAG and CTGCCCGGAGACCTGTCTCAGTGTGATCGTCTCCTCAGTTCAG) and XdownF and XdownR (CTGAACTGAGGAGCGATCACACTGAGACAAGTCTCGGGGCGAG and ATGCAAGCTTGTCTGATAGCGGATTCCGAGC) were used to amplify the regions flanking RSP\_0255, fused via PCR, digested and cloned into the BamHI and HindIII sites of *pk18mobsacB*. For unknown reasons, the regions flanking *pufY* (RSP\_7571, [<https://www.ncbi.nlm.nih.gov/protein/AGY32442>]) could not be fused by the same method, so a 1-kbp synthesized DNA fragment (Geneviz, Germany), comprised of two 500-bp regions identical to the upstream and downstream DNA sequences flanking RSP\_7571, was digested and cloned into the same sites of the *pk18mobsacB* vector as detailed above. The resulting plasmids were transferred from *Escherichia* (*E.*) *coli* S17-1 $\lambda$ pir cells to *Rba. sphaeroides* by conjugation. Selection of transconjugants was performed on M22 agar containing 30  $\mu$ g  $mL^{-1}$  kanamycin, and second recombinants were isolated on M22 medium containing 10% (w/v) sucrose. Successful generation of  $\Delta$ *pufX* and  $\Delta$ *pufY* strains was confirmed using PCR using Q5 High-Fidelity DNA Polymerase (New England Biolabs, UK) and DNA sequencing (Eurofins).

**Purification of RC-LH1 complexes.** The cells were harvested by centrifugation at 5000  $\times g$  for 10 min at 4 °C, washed twice with Tris-HCl (pH 8.0), and resuspended in working buffer (20 mM HEPES-Na, pH 8.0). Cells were disrupted by passage through a French press three times at 16,000 psi. Cell debris was removed by centrifugation at 20,000  $\times g$  for 30 min. Membranes were collected by centrifuging the resulting supernatant at 125,000  $\times g$  for 90 min and were solubilized by addition of  $\beta$ -DDM (n-dodecyl  $\beta$ -D-maltoside) to a final concentration of 3% (w/v) for 15 min to 1 h in the dark at 4 °C with gentle stirring. After the unsolubilized material was removed by centrifugation at 21,000  $\times g$  for 30 min, the clarified supernatant containing solubilized photosynthetic complexes was applied onto the 10–30% or 10–25% (w/v) continuous sucrose gradients made with working buffer containing 0.01% (w/v)  $\beta$ -DDM. Gradients were centrifuged at 230,000  $\times g$  for 18 h. For the WT dimers, a milder detergent  $\alpha$ -DDM (n-dodecyl  $\alpha$ -D-maltoside) was used in the isolation of RC-LH1 complexes, which includes a further purification step using a Superose 6 gel filtration column (GE). The purity of the RC-LH1 complex was characterized by sodium dodecyl sulfate-polyacrylamide gel electrophoresis (SDS-PAGE) (Fig. S1b; see also Source data file). Bands of proteins smaller than 15 kD were cut and analyzed by LC-MS/MS as described below, to identify the PufY peptide. For the WT monomers and mutants, the RC-LH1 complexes were

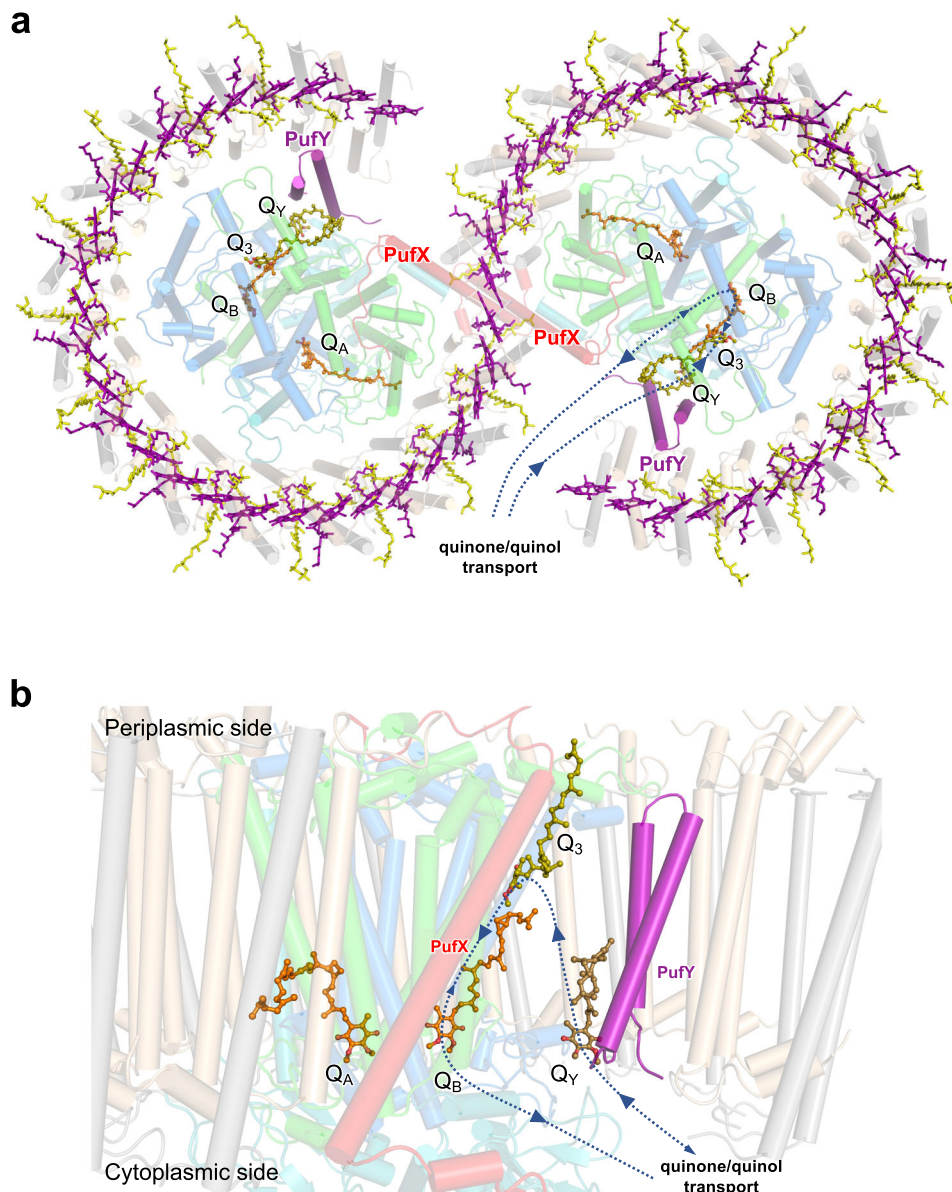


**Fig. 5** Quinone exchange pathways in the RC-LH1-PufX-PufY dimer as suggested by cryo-EM structures and computational simulations. **a** Periplasmic view of the locations of quinones ( $Q_A$ ,  $Q_B$ ,  $Q_3$ , and  $Q_Y$ ) in the RC-LH1 dimer. The arrows indicate the quinone/quinol diffusion pathways through the large opening in the LH1 ring, which is formed by PufX and PufY. **b** Side view of the quinone transport route through the  $Q_Y$ ,  $Q_3$ , and  $Q_B$  molecules. The pathways indicated by larger arrows are verified by CGMD simulations (Fig. S32, Movies S2-S4).

collected and concentrated using Vivaspin 6 100,000 MWCO columns (Cytiva) for heavy complexes (dimers) and Vivaspin 6 50,000 MWCO columns for light complexes (monomers). Simultaneously, the buffer containing sucrose was exchanged to working buffer containing 0.01% (w/v)  $\beta$ -DDM.

**Cryo-EM data collection.** A 3.0- $\mu$ L aliquot of the RC-LH1 complex was applied onto the holey carbon grid (300M-Au-R1.2/1.3; Beijing EBO Technology Limited) glow-discharged for 45 s for WT dimers, or the copper grids (Quantifoil R1.2/1.3 Cu, 300 mesh) with a thin carbon-supported film glow-discharged for 70 s for the WT monomers,  $\Delta pufX$  monomers, and  $\Delta pufY$  RC-LH1. The grids were plunge-frozen into liquid ethane using a Vitrobot Mark IV (Thermo Fisher Scientific). Parameters for plunge freezing were set as follows: blotting time of 3 s (WT monomer,  $\Delta pufY$  monomer,  $\Delta pufY$  dimers), 4 s (WT dimers) or 6 s ( $\Delta pufX$  monomers), waiting time of 30 s (WT dimers, WT monomer,  $\Delta pufY$  monomer,  $\Delta pufY$  dimer) or 3 s ( $\Delta pufX$  monomer), blotting force level of 0 ( $\Delta pufY$  monomer,  $\Delta pufY$  dimers), 4 (WT dimers) or -10 (WT monomer,  $\Delta pufX$  monomer), humidity 100%, chamber temperature 4 °C.

For the *Rba. sphaeroides* WT dimers, the micrographs were collected on a 300 kV Titan Krios microscope (Thermo Fisher Scientific) equipped with a K2

Summit direct electron detector (Gatan) at the Center for Biological Imaging, Core Facilities for Protein Science at the Institute of Biophysics, Chinese Academy of Sciences. Automated data acquisition was facilitated at a 130,000 magnification in super-resolution counting mode by SerialEM software. Images were recorded by beam-image shift data collection methods<sup>49</sup>. Each raw movie stack (32 frames) was captured using an exposure time of 6.4 s leading to a total dose of  $60 \text{ e}^-/\text{\AA}^2$  and a defocus value in the range from -1.8 to -2.2  $\mu\text{m}$ . A total of 6227 images were binned resulting in a pixel size of 1.04  $\text{\AA}$  for further data processing. Other RC-LH1 complexes were collected at the cryo-EM facility of RIKEN Center for Biosystems Dynamics Research (Yokohama) on a 300 kV Titan Krios equipped with a K3 Summit direct electron detector (Gatan) in counting mode, using EPU software. For the WT monomer, a total of 4700 movies were recorded at an 81,000 magnification and a pixel size of 1.06  $\text{\AA}$ . Each raw movie stack (48 frames) was captured by applying a total dose of  $45.026 \text{ e}^-/\text{\AA}^2$ . The defocus ranged from -0.7 to -1.8  $\mu\text{m}$ . For the  $\Delta pufX$  monomer, a total of 4807 movies were recorded at an 81,000 magnification and a pixel size of 1.06  $\text{\AA}$ . Each raw movie stack (48 frames) was captured by applying a total dose of  $46.549 \text{ e}^-/\text{\AA}^2$ . The defocus ranged from -0.8 to -1.8  $\mu\text{m}$ . For the  $\Delta pufY$  monomer, a total of 4700 movies were recorded at a 105,000 magnification and a pixel size of 0.8285  $\text{\AA}$ . Each raw movie stack (48 frames) was captured by applying a total dose of  $51.527 \text{ e}^-/\text{\AA}^2$ . The defocus ranged



from  $-0.8$  to  $-2.0$   $\mu\text{m}$ . For the  $\Delta\text{pufY}$  dimer, a total of 12,209 movies were recorded at a 105,000 magnification and a pixel size of  $0.8285$   $\text{\AA}$ . Each raw movie stack (48 frames) was captured by applying a total dose of  $50.868$   $\text{e}^-/\text{\AA}^2$ . The defocus ranged from  $-0.8$  to  $-2.0$   $\mu\text{m}$ .

**Data processing.** Collected movies were imported into RELION 3.0 or 3.1<sup>50,51</sup> and motion corrected using MotionCor2<sup>52</sup>. Contrast transfer function (CTF) parameters were determined by CTFIND-4.1<sup>53</sup> or Gctf<sup>54</sup>. For the WT dimers, a subset of particles was manually picked and processed with reference-free 2D classification, and the five 2D-class averages were selected as references for further automatic particle picking of the complete dataset, resulting in a total of 957,176 particles. 765,091 particles were selected for 3D classification after two rounds of reference-free 2D classification, which were classified into four classes using the initial model from the  $8$ - $\text{\AA}$  RC-LH1 complex of *Rba. sphaeroides* (PDB ID: 4V9G), which was lowpass filtered to a lower resolution of  $20$   $\text{\AA}$ . A total of 434,588 particles were kept for further two rounds of 3D classification with C2/C1 symmetry. Two distinct classes (145,392 particles for Class-1 and 147,085 particles for Class-2) were selected for 3D auto-refinement, CTF refinement, and Bayesian polishing, which resulted in the  $2.74$ - $\text{\AA}$  and  $2.90$ - $\text{\AA}$  density maps for Class-1 and Class-2, respectively.

For the WT monomer,  $\Delta\text{pufX}$  monomer,  $\Delta\text{pufY}$  monomer, and  $\Delta\text{pufY}$  dimer datasets, particles were picked automatically using SPHIRE-crYOLO<sup>55</sup>. The input box sizes were  $250 \times 250$  pixels for WT monomers and  $\Delta\text{pufX}$  monomers,  $300 \times 300$  pixels for  $\Delta\text{pufY}$  monomers, and  $400 \times 400$  pixels for  $\Delta\text{pufY}$  dimers. The total numbers of particles picked were 241,170 for WT monomers, 809,777 for  $\Delta\text{pufX}$  monomers, 241,170 for  $\Delta\text{pufY}$  monomers, and 373,025 for  $\Delta\text{pufY}$  dimers. Particles were then extracted in RELION 3.1 and subjected to reference-free 2D classifications. After each classification step, only the particles sorted into well-defined classes were selected to continue being processed. A 3D initial model was calculated in RELION 3.1 based on those particles and used as a reference for subsequent 3D classifications of selected particles. Once a well-defined 3D class was obtained, it was refined into a high-resolution electron potential map. The final selected particle numbers were 68,554 for WT monomers, 80,701 for  $\Delta\text{pufX}$  monomers, 56,391 for  $\Delta\text{pufY}$  monomers, 71,027 for  $\Delta\text{pufY}$  Type-1 dimers and 53,830 for  $\Delta\text{pufY}$  Type-2 dimers. Each map then went through several iterations of CTF parameter refinement, particle polishing, and 3D auto-refinement before it was corrected for the modulation transfer function (MTF) of the Gatan K3 summit camera and sharpened by RELION's post-processing job type. Based on the Fourier shell correlation (FSC)  $0.143$  criterion, the final global map resolutions were estimated to be  $2.79$   $\text{\AA}$  for WT monomers,  $6.62$   $\text{\AA}$  for  $\Delta\text{pufX}$  monomers,  $2.86$   $\text{\AA}$  for  $\Delta\text{pufY}$  monomers,  $3.08$   $\text{\AA}$  for  $\Delta\text{pufY}$  Type-1 dimers, and  $3.45$   $\text{\AA}$  for  $\Delta\text{pufY}$  Type-2 dimers. To improve the resolution of the  $\Delta\text{pufX}$  monomer, particles that made up the final map were further used to train Topaz<sup>56</sup> to recognize particles of interest, and particle picking was repeated using the trained Topaz. A total of 3,420,815 particles were picked, classified into reference-free 2D classes and subsequently into 3D classes until a well resolved 3D class was obtained. The final number of particles was 66,058 and the final map resolution was  $4.20$   $\text{\AA}$ . Local map resolutions were calculated by RELION 3.1.

**Model building and refinement.** Two copies of  $1.9$ - $\text{\AA}$  crystal structures of RC-LH1 from *Tch. tepidum* (PDB ID: 5Y5S) were initially docked into the  $2.74$ - $\text{\AA}$  resolution cryo-EM map of the WT Class-1 dimer using UCSF Chimera<sup>57</sup>. The amino acid sequences were further mutated to its counterparts in *Rba. sphaeroides* 2.4.1. PufY was identified as the protein RSP\_7571 through mass spectrometry (Fig. S22a, Data S1), which was further confirmed based on the perfect match of the specific sequence with the cryo-EM densities. The model of Class-1 was rebuilt manually basing on the cryo-EM density with COOT<sup>58</sup> and then real-space refined using Phenix 1.19.2<sup>59</sup> using C2 symmetry. The model of Class-2 was rebuilt and refined following the same procedure using the structure of Class-1 as the initial model. MolProbity<sup>460</sup> was used to evaluate the geometries of the structures. The atomic model of the WT monomer was built using the WT Class-2 dimer as a reference starting model. All amino acid sequences making up the models of WT monomer and dimers are listed in Fig. S33. The orientation of the SPO- $\beta$  molecules in the RC-LH1 complexes was tentatively assigned based on the resolutions of the WT monomer and Class-1 dimer structures. The models of  $\Delta\text{pufX}$  and  $\Delta\text{pufY}$  monomers were built using the WT monomer as a starting model and both  $\Delta\text{pufY}$  dimers were built using the WT Class-1 dimer as a starting model. The starting model structures were fit into experimental electron density maps as rigid bodies using UCSF Chimera. Three LH1 subunits were added to the starting structure of the  $\Delta\text{pufX}$  monomer and fitted into map, and PufX was removed. PufY was removed in all the  $\Delta\text{pufY}$  structures, and several LH1 subunits were removed in the  $\Delta\text{pufY}$  monomer and Type-2 dimer. These modifications were performed by using UCSF Chimera. Each structure was then adjusted manually using COOT. The final model was refined by Phenix 1.19.2, and the stereochemistry was assessed by MolProbity. Images were prepared with Chimera, ChimeraX<sup>61</sup>, and PyMOL<sup>62</sup> (Molecular Graphics System).

**Growth assays.** Three replicates of *Rba. sphaeroides* cultures were grown photo-trophically in 8 ml glass tubes as detailed above. The tubes were constantly rotated

using the RM-4D Rotator mixer (Premiere). Optical density at  $680$  nm was measured using a Colorimeter (WPA Colourwave CO7000).

**Absorption spectra.** Purified RC-LH1 complexes from sucrose gradient were collected and absorbance was measured from  $300$  to  $900$  nm in  $1$ -nm intervals using a Libra S22 spectrophotometer (Biochrom).

**Quinone analysis.** The quinones from the dimeric RC-LH1 samples were extracted using  $1:1$  methanol:chloroform (v:v) containing  $0.02\%$  (w/v)  $\text{FeCl}_3$ , and were injected into a Shimadzu 20A HPLC system employing a Shim-pack GIST C-18 reversed-phase column ( $4.6$  mm  $\times$   $250$  mm). The column was pre-equilibrated and was then eluted with  $8:2$  methanol:isopropanol (v:v) at a flow rate of  $1$  mL  $\text{min}^{-1}$  for  $1$  h at  $40$   $^\circ\text{C}$ . The elution was analyzed by an LC-20AT detector (Shimadzu), monitored at  $275$  nm. Ubiquinone-10 (UQ-10) was identified by comparing the retention time of the quinones from the RC-LH1 complexes with that of the UQ-10 standard (TargetMol, China, Cat No.: T2796).

**Liquid chromatography-mass spectrometry (LC-MS/MS) protein identification.** Gel bands containing the protein sample were manually excised. Each of the protein bands was then digested individually as below. The protein bands were cut into small plugs, washed twice in distilled water, and were then dehydrated in  $100\%$  acetonitrile for  $10$  min and dried in a SpeedVac (Labconco) for  $15$  min. Reduction ( $10$  mM DTT in  $25$  mM  $\text{NH}_4\text{HCO}_3$  for  $45$  min at  $56$   $^\circ\text{C}$ ) and alkylation ( $40$  mM iodoacetamide in  $25$  mM  $\text{NH}_4\text{HCO}_3$  for  $45$  min at room temperature in the dark) were performed, followed by washing with  $50\%$  acetonitrile in  $25$  mM  $\text{NH}_4\text{HCO}_3$  twice. The gel plugs were then dried using a SpeedVac and digested with sequence-grade modified trypsin ( $40$  ng for each band) in  $25$  mM  $\text{NH}_4\text{HCO}_3$  overnight at  $37$   $^\circ\text{C}$ . The enzymatic reaction was stopped by adding formic acid to a  $1\%$  final concentration. The solution was transferred for LC-MS/MS analysis.

LC-MS/MS analysis was performed using a nanoLC-LTQ-Orbitrap XL mass spectrometer (Thermo Scientific, San Jose, CA) in line with an Easy-nLC 1200 HPLC system. Tryptic peptides generated above were loaded onto a self-packed trap column (ReproSil-Pur C18-AQ,  $150$   $\mu\text{m}$  i.d.  $\times$   $2$  mm,  $5$   $\mu\text{m}$  particle) (Dr. Maisch GmbH, Ammerbuch) which was connected to the self-packed analytical column (ReproSil-Pur C18-AQ,  $75$   $\mu\text{m}$  i.d.  $\times$   $150$  mm,  $3$   $\mu\text{m}$  particle). The peptides were then eluted over a gradient ( $0$ – $36\%$  B in  $78$  min,  $36$ – $80\%$  B in  $12$  min, where A =  $\text{H}_2\text{O}$  with  $0.1\%$  formic acid and B =  $80\%$  acetonitrile with  $0.1\%$  formic acid) at a flow rate of  $300$  nL  $\text{min}^{-1}$  and introduced online into the linear ion trap mass spectrometer using nano electrospray ionization (ESI). Data-dependent scanning was incorporated to select the  $10$  most abundant ions (one microscan per spectra; precursor isolation width  $\pm 1.0$   $m/z$ ,  $35\%$  collision energy,  $30$  ms ion activation, exclusion duration:  $120$  s; repeat count:  $1$ ) from a full-scan mass spectrum ( $300$  to  $1600$   $m/z$  at res =  $60,000$ ) for fragmentation by collision induced dissociation (CID). Lock mass option was enabled for the  $462.14658$   $m/z$ .

MS data were analyzed using Proteome Discoverer (version 1.4.0.288, Thermo Scientific). MS2 spectra were searched against the UniProt proteome database of *Rhodobacter sphaeroides* 2.4.1 (UniProt ID: UP000002703) using the SEQUEST search engine. Peptides with and above  $+2$  charge states were accepted if they were fully enzymatic. The following residue modifications were allowed in the search: carbamidomethylation on cysteine and oxidation on methionine. Peptide tolerance of  $20$  ppm and fragment mass tolerance of  $0.6$  Da were applied. Peptide spectral matches (PSM) were validated by a targeted decoy database search at a  $1\%$  false discovery rate (FDR). Peptide identifications were grouped into proteins according to the law of parsimony.

**All-atom molecular dynamics (AAMD) simulations.** The structural model of the WT Class-1 RC-LH1 dimer was modified for AAMD simulations as follows. As some atoms of BChls *a*, BPhes and UQ-10 were missing in the cryo-EM structure due to poor density of their flexible tails, their complete structures were modeled manually. The two UQ-10 molecules that were assigned in the Class-2 dimer but absent in the Class-1 dimer were added in the Class-1 model at their respective positions. The positions of the lipids identified were determined based on electron densities, which cover most of the unassigned space between the RC and LH1 ring, especially at the periplasmic side of RC-LH1. At the cytoplasmic side, the remaining empty space was filled with lipid molecules modeled with their heads coordinated by Arg14 and Arg15 of LH1  $\alpha$ -chains. This arrangement was made based on: (1) the Arg residue favorably interacts with the phosphate head of a lipid, (2) LH1  $\alpha$ -Arg14 and Arg15 are at the same altitude as the heads of those lipid molecules modeled on the cytoplasmic side of the complex based on density, and (3) Arg residues also form a specific polar local environment around lipid heads in the structure. In total, additional  $22$  1,2-distearoyl-*sn*-glycero-3-phosphocholine (DSPC) molecules were modeled manually to fill the spaces between the RC and LH1 ring of each monomer. The quality of the manually modeled sections of the membrane to study quinone dynamics in membrane environment was verified by the inability of water molecules to penetrate inside the bilayer (Fig. S34).

The dimeric structure was divided into two monomers and the position of the lipid bilayer of each monomer was predicted by the Positioning of Proteins in Membrane (PPM) server<sup>63</sup>. The monomer structures were superposed on the dimeric structure to calculate the positions of the lipid bilayers in the dimer. The average vector of the

normal vectors of the two lipid-bilayer surfaces was calculated. The dimeric structure was translated and rotated, so that the geometric center was at the origin and the average vector was aligned to the Z axis. The dimeric structure was then embedded in a solvated lipid bilayer using the “Membrane Builder” function<sup>64</sup> of the CHARMM-GUI server<sup>65</sup>. The generated system was composed of 66 protein chains, 64 BChls *a*, 4 BPhes, 2 tetraoleoyl cardiolipin (TSCL), 52 SPOs, 8 UQ-10, 38 DSPC, and 1375 1-palmitoyl-2-oleoyl-*sn*-glycero-3-phosphocholine (POPC) molecules, as well as 2 Fe<sup>2+</sup>, 544 K<sup>+</sup>, 573 Cl<sup>-</sup> ions, and 195,489 water molecules. The total number of atoms was 868,355 and the size of the initial system was 25.6 nm × 25.6 nm × 14.1 nm. The same topologies and parameters as those used in the previous study<sup>17</sup> were used for BChls *a*, BPhes, and SPOs. The topology and the parameters of TSCL (Data S2) were created by modifying those of tetraoleoyl cardiolipin provided by the CHARMM-GUI server. Distances between the metal ions (Mg<sup>2+</sup> and Fe<sup>2+</sup>) and their coordinating atoms were restrained with a force constant of 1.0 × 10<sup>5</sup> kJ nm<sup>-2</sup>. The TIP3P model<sup>66</sup> was used for water molecules. The CHARMM36m force field<sup>6</sup> was used for the protein chains and the CHARMM36 force field<sup>67–69</sup> was used for other molecules.

After the system was energy-minimized, the system was equilibrated in nine steps. In the first two steps, the system was equilibrated for 0.25 ns in the NVT ensemble, and in successive three steps, it was equilibrated for 1.125 ns in the NPT ensembles. In these steps, the positions of the protein and the ligand non-hydrogen atoms were restrained to their initial positions. The force constants were gradually decreased from 4000 to 1000 kJ mol<sup>-1</sup> nm<sup>-2</sup> for the protein backbone and the ligand atoms and from 2000 to 500 kJ mol<sup>-1</sup> nm<sup>-2</sup> for the protein sidechain atoms. The Z coordinates of the phosphorus atoms of the POPC molecules were also restrained with the force constants from 1000 to 40 kJ mol<sup>-1</sup> nm<sup>-2</sup>. In the sixth step, a 40-ns MD simulation was performed with the position restraints of 1000 kJ mol<sup>-1</sup> nm<sup>-2</sup> for the protein backbone and the ligand atoms and of 500 kJ mol<sup>-1</sup> nm<sup>-2</sup> for the protein sidechain atoms. No restraints were imposed on the lipid atoms. In the last three steps, an MD simulation was performed for 1.5 ns in total. The force constants were gradually decreased to 50 kJ mol<sup>-1</sup> nm<sup>-2</sup> for the protein backbone and the ligand atoms and 0 kJ mol<sup>-1</sup> nm<sup>-2</sup> for the protein sidechain atoms. Finally, a 500-ns production MD simulation was performed without restraints. The temperature was kept at 303.15 K throughout the MD simulations and the pressure was kept at 1.0 × 10<sup>5</sup> Pa except for the first two equilibration steps. In the equilibration steps, the Berendsen weak coupling method<sup>70</sup> was used to control the temperature and the pressure. In the production run, the Nosé-Hoover method<sup>71,72</sup> and the Parrinello-Rahman method<sup>73,74</sup> were used to control them, respectively. Bond lengths involving hydrogen atoms were constrained using the LINCS algorithm<sup>75,76</sup> to allow the use of a large time step (2 fs). Electrostatic interactions were calculated with the particle mesh Ewald method<sup>77,78</sup>. All AAMD simulations were performed using GROMACS 2021<sup>79</sup>, with coordinates recorded every 10 ps. As illustrated in Fig. S35, the structure of the RC-LH1 dimer and the size of the LH1 opening did not change significantly and no notable change in the lipid arrangement within the RC-LH1 structure was observed after simulations.

**Coarse-grained molecular dynamics (CGMD) simulations.** CGMD simulations were performed for the whole dimer structure and the UQ-10-free structure. The former is referred to as “UQ-10-bound simulation”. In the latter simulation, all the UQ-10 molecules were removed from the dimer structure and 60 UQ-10 molecules were randomly placed around the dimer as described below to investigate the UQ-10-binding process. Therefore, the latter simulation is referred to as “UQ-10-binding simulation”. The coarse-grained (CG) models were constructed using the MARTINI 2.2 force field<sup>80</sup>. The CG parameters of UQ-10, DSPC, and POPC were taken from literatures<sup>81,82</sup>. The parameters of the coarse-grained models of BChls, BPhes, and TSCL were created by modifying those of chlorophyll *a*<sup>81</sup>, pheophytin *a*<sup>81</sup>, and tetraoleoyl cardiolipin<sup>83</sup>, respectively (for detail, see Supplementary Methods and Fig. S36). The parameters of SPO (Data S3) were determined so that the CG model reproduced the dynamics observed in AAMD and the water-octanol partition coefficient predicted by the XLOGP3 program<sup>84</sup>. The ElnDyn model<sup>85</sup> was used to construct the CG models of protein chains and to maintain the quaternary structure of the dimer with an elastic network. All the backbone beads of the protein, the SP3 beads of BChls and BPhes and all the beads of SPOs were mutually connected by springs when the distance between a bead pair was within 9 Å. The force constants were 500 kJ mol<sup>-1</sup> nm<sup>-2</sup> for the backbone bead pairs and 100 kJ mol<sup>-1</sup> nm<sup>-2</sup> for the other pairs. In addition, the sidechain beads of proteins within 3.5 Å from the Mg<sup>2+</sup> ions of BChls were connected with the Mg<sup>2+</sup> ions by springs with a force constant of 500 kJ mol<sup>-1</sup> nm<sup>-2</sup> to maintain the coordination structure. Each of the whole (i.e., UQ-10-bound) and the UQ-10-free structures was embedded in a solvated lipid bilayer using the CHARMM-GUI server<sup>65,86</sup>. Each solvated lipid bilayer was composed of ~2000 POPC molecules, 59,000 CG waters, and 0.15 M Na<sup>+</sup>/Cl<sup>-</sup> ions that neutralized the net charge of the system. After energy minimization, each system was equilibrated for 1 μs in the NPT ensemble. During the equilibration, the positional restraints were imposed on the protein backbone beads (for both the systems) and the UQ-10 beads (for the system with the UQ-10-bound structure). For the UQ-10-binding simulation, 60 POPC molecules in the system with the UQ-10-free structure farther than 140 Å from the center of mass of the dimer were randomly replaced by UQ-10 molecules. The system was energy-minimized and equilibrated for 100 ps with the positional restraints imposed on the protein backbone beads. For each system, a production

run was performed for 5 μs in the NPT ensembles. The temperature was kept at 303.15 K using the velocity-rescaling method<sup>87</sup> with coupling constants of 1.0 ps. The pressure was kept at 1.0 × 10<sup>5</sup> Pa using the Parrinello-Rahman method<sup>73,74</sup> with coupling constants of 12.0 ps. Electrostatic interactions were calculated using the reaction-field method<sup>88</sup> with a cutoff of 1.1 nm. Van der Waals interactions were calculated with a modified Lennard-Jones potential, where the potential was shifted to zero at the cut-off distance of 1.1 nm. Bond lengths specified in the MARTINI force field were constrained using the LINCS algorithm. The time step was 20 fs. All the CGMD simulations were performed using GROMACS 2019.

**Reporting summary.** Further information on research design is available in the Nature Research Reporting Summary linked to this article.

## Data availability

The cryo-EM density maps were deposited in the Electron Microscopy Data Bank (EMDB, [www.ebi.ac.uk/pdbe/emdb/](http://www.ebi.ac.uk/pdbe/emdb/)) under the following accession codes: EMD-32058 for WT Class-1 dimer, EMD-32059 for WT Class-2 dimer, EMD-32047 for WT monomer, EMD-32062 for Δ*pufX* monomer, EMD-32042 for Δ*pufY* monomer, EMD-31835 for Δ*pufY* Type-1 dimer, and EMD-31875 for Δ*pufY* Type-2 dimer. The atomic coordinates have been deposited in the Protein Data Bank (PDB, [www.rcsb.org](http://www.rcsb.org)) under the following accession codes: WT Class-1 dimer, 7VOR; WT Class-2 dimer, 7VOT; WT monomer, 7VNY; Δ*pufX* monomer, 7VOY; Δ*pufY* monomer, 7VNM; Δ*pufY* Type-1 dimer, 7VA9; Δ*pufY* Type-2 dimer, 7VB9. The data of processing cryo-EM images and electron density maps are provided in Supplementary Information and Source data file. All other data generated or analyzed are available from the corresponding authors on reasonable request. Source data are provided with this paper.

Received: 28 October 2021; Accepted: 22 March 2022;

Published online: 13 April 2022

## References

- Mullineaux, C. W. & Liu, L. N. Membrane dynamics in phototrophic bacteria. *Annu. Rev. Microbiol.* **74**, 633–654 (2020).
- Gardiner, A. T., Nguyen-Phan, T. C. & Cogdell, R. J. A comparative look at structural variation among RC-LH1 ‘Core’ complexes present in anoxygenic phototrophic bacteria. *Photosynth. Res.* **145**, 83–96 (2020).
- Miller, L. C., Zhao, L., Canniffe, D. P., Martin, D. & Liu, L. N. Unfolding pathway and intermolecular interactions of the cytochrome subunit in the bacterial photosynthetic reaction center. *Biochim. Biophys. Acta - Bioenerg.* **1861**, 148204 (2020).
- Liu, L. N., Duquesne, K., Oesterheld, F., Sturgis, J. N. & Scheuring, S. Forces guiding assembly of light-harvesting complex 2 in native membranes. *Proc. Natl Acad. Sci. USA* **108**, 9455–9459 (2011).
- Miller, L. C., Martin, D. S., Liu, L.-N. & Canniffe, D. P. Composition, organisation and function of purple photosynthetic machinery. In *Microbial Photosynthesis* (ed. Wang, Q.) 73–114 (Springer Singapore, 2020).
- Singharoy, A. et al. Atoms to phenotypes: molecular design principles of cellular energy metabolism. *Cell* **179**, 1098–1111 e1023 (2019).
- Niwa, S. et al. Structure of the LH1-RC complex from *Thermochromatium tepidum* at 3.0 Å. *Nature* **508**, 228–232 (2014).
- Yu, L. J., Suga, M., Wang-Otomo, Z. Y. & Shen, J. R. Structure of photosynthetic LH1-RC supercomplex at 1.9 Å resolution. *Nature* **556**, 209–213 (2018).
- Tani, K. et al. Cryo-EM structure of a Ca<sup>2+</sup>-bound photosynthetic LH1-RC complex containing multiple alphabeta-polypeptides. *Nat. Commun.* **11**, 4955 (2020).
- Qian, P. et al. Cryo-EM structure of the *Rhodospirillum rubrum* RC-LH1 complex at 2.5 Å. *Biochem. J.* **478**, 3253–3263 (2021).
- Tani, K. et al. Cryo-EM Structure of the Photosynthetic LH1-RC Complex from *Rhodospirillum rubrum*. *Biochemistry* **60**, 2483–2491 (2021).
- Qian, P., Siebert, C. A., Wang, P., Canniffe, D. P. & Hunter, C. N. Cryo-EM structure of the *Blastochloris viridis* LH1-RC complex at 2.9 Å. *Nature* **556**, 203–208 (2018).
- Roszak, A. W. et al. Crystal structure of the RC-LH1 core complex from *Rhodospseudomonas palustris*. *Science* **302**, 1969–1972 (2003).
- Xin, Y. et al. Cryo-EM structure of the RC-LH core complex from an early branching photosynthetic prokaryote. *Nat. Commun.* **9**, 1568 (2018).
- Busselez, J. et al. Structural basis for the PufX-mediated dimerization of bacterial photosynthetic core complexes. *Structure* **15**, 1674–1683 (2007).
- Swainsbury, D. J. K. et al. Structures of *Rhodospseudomonas palustris* RC-LH1 complexes with open or closed quinone channels. *Sci. Adv.* **7**, eabe2631 (2021).
- Bracun, L. et al. Cryo-EM structure of the photosynthetic RC-LH1-PufX supercomplex at 2.8-Å resolution. *Sci. Adv.* **7**, eabf8864 (2021).

18. Qian, P. et al. Three-dimensional structure of the *Rhodobacter sphaeroides* RC-LH1-PufX complex: dimerization and quinone channels promoted by PufX. *Biochemistry* **52**, 7575–7585 (2013).
19. Qian, P., Hunter, C. N. & Bullough, P. A. The 8.5 Å projection structure of the core RC-LH1-PufX dimer of *Rhodobacter sphaeroides*. *J. Mol. Biol.* **349**, 948–960 (2005).
20. Qian, P., Bullough, P. A. & Hunter, C. N. Three-dimensional reconstruction of a membrane-bending complex: the RC-LH1-PufX core dimer of *Rhodobacter sphaeroides*. *J. Biol. Chem.* **283**, 14002–14011 (2008).
21. Jungas, C., Ranck, J. L., Rigaud, J. L., Joliet, P. & Verméglio, A. Supramolecular organization of the photosynthetic apparatus of *Rhodobacter sphaeroides*. *EMBO J.* **18**, 534–542 (1999).
22. Siebert, C. A. et al. Molecular architecture of photosynthetic membranes in *Rhodobacter sphaeroides*: the role of PufX. *EMBO J.* **23**, 690–700 (2004).
23. Scheuring, S. et al. Structural role of PufX in the dimerization of the photosynthetic core complex of *Rhodobacter sphaeroides*. *J. Biol. Chem.* **279**, 3620–3626 (2004).
24. Bahatyrova, S. et al. The native architecture of a photosynthetic membrane. *Nature* **430**, 1058–1062 (2004).
25. Liu, L. N. & Scheuring, S. Investigation of photosynthetic membrane structure using atomic force microscopy. *Trends Plant Sci.* **18**, 277–286 (2013).
26. Koepke, J. et al. pH modulates the quinone position in the photosynthetic reaction center from *Rhodobacter sphaeroides* in the neutral and charge separated states. *J. Mol. Biol.* **371**, 396–409 (2007).
27. Olsen, J. D., Martin, E. C. & Hunter, C. N. The PufX quinone channel enables the light-harvesting 1 antenna to bind more carotenoids for light collection and photoprotection. *FEBS Lett.* **591**, 573–580 (2017).
28. Chenchiliyan, M. et al. Dimerization of core complexes as an efficient strategy for energy trapping in *Rhodobacter sphaeroides*. *Biochim. Biophys. Acta* **1857**, 634–642 (2016).
29. Barz, W. P. et al. Role of the PufX protein in photosynthetic growth of *Rhodobacter sphaeroides*. 2. PufX is required for efficient ubiquinone/ubiquinol exchange between the reaction center QB site and the cytochrome *bcl* complex. *Biochemistry* **34**, 15248–15258 (1995).
30. Lilburn, T. G., Haith, C. E., Prince, R. C. & Beatty, J. T. Pleiotropic effects of *pufX* gene deletion on the structure and function of the photosynthetic apparatus of *Rhodobacter capsulatus*. *Biochim. Biophys. Acta* **1100**, 160–170 (1992).
31. Scheuring, S., Busselez, J. & Levy, D. Structure of the dimeric PufX-containing core complex of *Rhodobacter blasticus* by in situ atomic force microscopy. *J. Biol. Chem.* **280**, 1426–1431 (2005).
32. Semchonok, D. A., Chauvin, J. P., Frese, R. N., Jungas, C. & Boekema, E. J. Structure of the dimeric RC-LH1-PufX complex from *Rhodobacter bogoriensis* investigated by electron microscopy. *Philos. Trans. R. Soc. Lond. B Biol. Sci.* **367**, 3412–3419 (2012).
33. Crouch, L. I. & Jones, M. R. Cross-species investigation of the functions of the *Rhodobacter* PufX polypeptide and the composition of the RC-LH1 core complex. *Biochim. Biophys. Acta* **1817**, 336–352 (2012).
34. Qian, P., Martin, E. C., Ng, I. W. & Hunter, C. N. The C-terminus of PufX plays a key role in dimerisation and assembly of the reaction center light-harvesting 1 complex from *Rhodobacter sphaeroides*. *Biochim. Biophys. Acta-Bioenerg.* **1858**, 795–803 (2017).
35. Ratcliffe, E. C. et al. Experimental evidence that the membrane-spanning helix of PufX adopts a bent conformation that facilitates dimerisation of the *Rhodobacter sphaeroides* RC-LH1 complex through N-terminal interactions. *Biochim. Biophys. Acta* **1807**, 95–107 (2011).
36. Francia, F., Wang, J., Zischka, H., Venturoli, G. & Oesterheld, D. Role of the N- and C-terminal regions of the PufX protein in the structural organization of the photosynthetic core complex of *Rhodobacter sphaeroides*. *Eur. J. Biochem.* **269**, 1877–1885 (2002).
37. Farchaus, J. W., Barz, W. P., Grunberg, H. & Oesterheld, D. Studies on the expression of the *pufX* polypeptide and its requirement for photoheterotrophic growth in *Rhodobacter sphaeroides*. *EMBO J.* **11**, 2779–2788 (1992).
38. Adams, P. G., Mothersole, D. J., Ng, I. W., Olsen, J. D. & Hunter, C. N. Monomeric RC-LH1 core complexes retard LH2 assembly and intracytoplasmic membrane formation in PufX-minus mutants of *Rhodobacter sphaeroides*. *Biochim. Biophys. Acta* **1807**, 1044–1055 (2011).
39. Walz, T., Jamieson, S. J., Bowers, C. M., Bullough, P. A. & Hunter, C. N. Projection structures of three photosynthetic complexes from *Rhodobacter sphaeroides*: LH2 at 6 Å, LH1 and RC-LH1 at 25 Å. *J. Mol. Biol.* **282**, 833–845 (1998).
40. McGlynn, P., Hunter, C. N. & Jones, M. R. The *Rhodobacter sphaeroides* PufX protein is not required for photosynthetic competence in the absence of a light harvesting system. *FEBS Lett.* **349**, 349–353 (1994).
41. Olsen, J. D. et al. Aberrant assembly complexes of the reaction center light-harvesting 1 PufX (RC-LH1-PufX) core complex of *Rhodobacter sphaeroides* imaged by atomic force microscopy. *J. Biol. Chem.* **289**, 29927–29936 (2014).
42. Tani, K. et al. A previously unrecognized membrane protein in the *Rhodobacter sphaeroides* LH1-RC photocore. *Nat. Commun.* **12**, 6300 (2021).
43. Qian, P. et al. Cryo-EM structure of the monomeric *Rhodobacter sphaeroides* RC-LH1 core complex at 2.5 Å. *Biochem. J.* **478**, 3775–3790 (2021).
44. Pugh, R. J., McGlynn, P., Jones, M. R. & Hunter, C. N. The LH1-RC core complex of *Rhodobacter sphaeroides*: interaction between components, time-dependent assembly, and topology of the PufX protein. *Biochim. Biophys. Acta* **1366**, 301–316 (1998).
45. Scheuring, S. et al. The architecture of *Rhodobacter sphaeroides* chromatophores. *Biochim. Biophys. Acta* **1837**, 1263–1270 (2014).
46. Qian, P. et al. Cryo-EM structure of the dimeric *Rhodobacter sphaeroides* RC-LH1 core complex at 2.9 Å: the structural basis for dimerisation. *Biochem. J.* **478**, 3923–3937 (2021).
47. Gubellini, F., Francia, F., Busselez, J., Venturoli, G. & Lévy, D. Functional and structural analysis of the photosynthetic apparatus of *Rhodobacter veldkampii*. *Biochemistry* **45**, 10512–10520 (2006).
48. Jackson, P. J. et al. Identification of protein W, the elusive sixth subunit of the *Rhodospseudomonas palustris* reaction center-light harvesting 1 core complex. *Biochim. Biophys. Acta Bioenerg.* **1859**, 119–128 (2018).
49. Wu, C., Huang, X., Cheng, J., Zhu, D. & Zhang, X. High-quality, high-throughput cryo-electron microscopy data collection via beam tilt and astigmatism-free beam-image shift. *J. Struct. Biol.* **208**, 107396 (2019).
50. Zivanov, J. et al. New tools for automated high-resolution cryo-EM structure determination in RELION-3. *Elife* **7**, e42166 (2018).
51. Zivanov, J., Nakane, T. & Scheres, S. H. W. Estimation of high-order aberrations and anisotropic magnification from cryo-EM data sets in RELION-3.1. *IUCr* **7**, 253–267 (2020).
52. Zheng, S. Q. et al. MotionCor2: anisotropic correction of beam-induced motion for improved cryo-electron microscopy. *Nat. Methods* **14**, 331–332 (2017).
53. Rohou, A. & Grigorieff, N. CTFFIND4: Fast and accurate defocus estimation from electron micrographs. *J. Struct. Biol.* **192**, 216–221 (2015).
54. Zhang, K., Gctf & Real-time, C. T. F. determination and correction. *J. Struct. Biol.* **193**, 1–12 (2016).
55. Wagner, T. et al. SPHIRE-crYOLO is a fast and accurate fully automated particle picker for cryo-EM. *Commun. Biol.* **2**, 218 (2019).
56. Bepler, T. et al. Positive-unlabeled convolutional neural networks for particle picking in cryo-electron micrographs. *Res. Comput. Mol. Biol.* **10812**, 245–247 (2018).
57. Pettersen, E. F. et al. UCSF Chimera—a visualization system for exploratory research and analysis. *J. Comput. Chem.* **25**, 1605–1612 (2004).
58. Casanal, A., Lohkamp, B. & Emsley, P. Current developments in Coot for macromolecular model building of Electron Cryo-microscopy and Crystallographic Data. *Protein Sci.* **29**, 1069–1078 (2020).
59. Liebschner, D. et al. Macromolecular structure determination using X-rays, neutrons and electrons: recent developments in Phenix. *Acta Crystallogr. D. Struct. Biol.* **75**, 861–877 (2019).
60. Williams, C. J. et al. MolProbity: more and better reference data for improved all-atom structure validation. *Protein Sci.* **27**, 293–315 (2018).
61. Pettersen, E. F. et al. UCSF ChimeraX: structure visualization for researchers, educators, and developers. *Protein Sci.* **30**, 70–82 (2021).
62. Lilkova, E. et al. *The PyMOL Molecular Graphics System*, Version 2.0 (Schrodinger, LLC, 2015).
63. Lomize, M. A., Pogozheva, I. D., Joo, H., Mosberg, H. I. & Lomize, A. L. OPM database and PPM web server: resources for positioning of proteins in membranes. *Nucleic Acids Res.* **40**, D370–D376 (2012).
64. Wu, E. L. et al. CHARMM-GUI membrane builder toward realistic biological membrane simulations. *J. Comput. Chem.* **35**, 1997–2004 (2014).
65. Jo, S., Kim, T., Iyer, V. G. & Im, W. CHARMM-GUI: A web-based graphical user interface for CHARMM. *J. Comput. Chem.* **29**, 1859–1865 (2008).
66. Jorgensen, W. L., Chandrasekhar, J., Madura, J. D., Impey, R. W. & Klein, M. L. Comparison of simple potential functions for simulating liquid water. *J. Chem. Phys.* **79**, 926–935 (1983).
67. Best, R. B. et al. Optimization of the additive CHARMM all-atom protein force field targeting improved sampling of the backbone  $\phi$ ,  $\psi$  and side-chain  $\chi_1$  and  $\chi_2$  dihedral angles. *J. Chem. Theory Comput.* **8**, 3257–3273 (2012).
68. Klauda, J. B. et al. Update of the CHARMM all-atom additive force field for lipids: validation on six lipid types. *J. Phys. Chem. B* **114**, 7830–7843 (2010).
69. Vanommeslaeghe, K. et al. CHARMM general force field: a force field for drug-like molecules compatible with the CHARMM all-atom additive biological force fields. *J. Comput. Chem.* **31**, 671–690 (2010).
70. Berendsen, H. J. C., Postma, J. P. M., Vangunsteren, W. F., Dinola, A. & Haak, J. R. Molecular dynamics with coupling to an external bath. *J. Chem. Phys.* **81**, 3684–3690 (1984).
71. Hoover, W. G. Canonical dynamics: equilibrium phase-space distributions. *Phys. Rev. A* **31**, 1695–1697 (1985).

72. Nose, S. A molecular dynamics method for simulations in the canonical ensemble. *Mol. Phys.* **52**, 255–268 (1984).
73. Parrinello, M. & Rahman, A. Polymorphic transitions in single crystals: a new molecular dynamics method. *J. Appl. Phys.* **52**, 7182–7190 (1981).
74. Nose, S. & Klein, M. L. Constant pressure molecular dynamics for molecular systems. *Mol. Phys.* **50**, 1055–1076 (1983).
75. Hess, B. P-LINCS: a parallel linear constraint solver for molecular simulation. *J. Chem. Theory Comput.* **4**, 116–122 (2008).
76. Hess, B., Bekker, H., Berendsen, H. J. C. & Fraaije, J. G. E. M. LINCS: a linear constraint solver for molecular simulations. *J. Comput. Chem.* **18**, 1463–1472 (1997).
77. Essmann, U. et al. A smooth particle mesh Ewald method. *J. Chem. Phys.* **103**, 8577–8593 (1995).
78. Darden, T., York, D. & Pedersen, L. Particle mesh Ewald: an  $N$ -log( $N$ ) method for Ewald sums in large systems. *J. Chem. Phys.* **98**, 10089–10092 (1993).
79. Hess, B., Kutzner, C., van der Spoel, D. & Lindahl, E. GROMACS 4: algorithms for highly efficient, load-balanced, and scalable molecular simulation. *J. Chem. Theory Comput.* **4**, 435–447 (2008).
80. Marrink, S. J., Risselada, H. J., Yefimov, S., Tieleman, D. P. & de Vries, A. H. The MARTINI force field: coarse grained model for biomolecular simulations. *J. Phys. Chem. B* **111**, 7812–7824 (2007).
81. de Jong, D. H. et al. Atomistic and coarse grain topologies for the cofactors associated with the photosystem II core complex. *J. Phys. Chem. B* **119**, 7791–7803 (2015).
82. Wassenaar, T. A., Ingólfsson, H. I., Bockmann, R. A., Tieleman, D. P. & Marrink, S. J. Computational lipidomics with insane: a versatile tool for generating custom membranes for molecular simulations. *J. Chem. Theory Comput.* **11**, 2144–2155 (2015).
83. Dahlberg, M. & Maliniak, A. Mechanical properties of coarse-grained bilayers formed by cardiolipin and zwitterionic lipids. *J. Chem. Theory Comput.* **6**, 1638–1649 (2010).
84. Cheng, T. J. et al. Computation of octanol-water partition coefficients by guiding an additive model with knowledge. *J. Chem. Inf. Modeling* **47**, 2140–2148 (2007).
85. Periolo, X., Cavalli, M., Marrink, S. J. & Ceruso, M. A. Combining an elastic network with a coarse-grained molecular force field: structure, dynamics, and intermolecular recognition. *J. Chem. Theory Comput.* **5**, 2531–2543 (2009).
86. Lee, J. et al. CHARMM-GUI INput Generator for NAMD, GROMACS, AMBER, OpenMM, and CHARMM/OpenMM simulations using the CHARMM36 additive force field. *J. Chem. Theory Comput.* **12**, 405–413 (2016).
87. Bussi, G., Donadio, D. & Parrinello, M. Canonical sampling through velocity rescaling. *J. Chem. Phys.* **126**, 014101 (2007).
88. Tironi, I. G., Sperb, R., Smith, P. E. & Vangunsteren, W. F. A generalized reaction field method for molecular dynamics simulations. *J. Chem. Phys.* **102**, 5451–5459 (1995).
89. Russ, W. P. & Engelman, D. M. The GxxxG motif: a framework for transmembrane helix-helix association. *J. Mol. Biol.* **296**, 911–919 (2000).

## Acknowledgements

We thank B.L. Zhu, X.J. Huang, L.H. Chen, X.J. Li, G. Ji, D.Y. Fan, B.X. Huangpu, T.X. Niu, F. Sun, and other staff members at the Center for Biological Imaging (IBP, CAS) for the technical support in EM data collection; X. Ding, Z.S. Xie, L.L. Niu, N.L. Zhu, M.M. Zhang, and F.Q. Yang for mass spectrometer; X.D. Su, L. Si, X.L. Zhao, H.M. Zhang, and L.F. Shi for the assistance in sample preparation and data collection. Cryo-EM data of native dimers were collected at the Center for Biological Imaging, Core Facilities for Protein Science at the Institute of Biophysics (IBP), Chinese Academy of Sciences (CAS).

Cryo-EM of the other complexes were collected at the cryo-EM facility of the RIKEN Center for Biosystems Dynamics Research (Yokohama). This work was supported by the Strategic Priority Research Program of CAS (XDB27020106 to M.L. and XDB37020101 to P.C.), the National Natural Science Foundation of China (32070259 to P.C., 31930064 to M.L., 32070109 to L.-N.L.), the National Key R&D Program of China (2021YFA0909600 to L.-N.L.), the Royal Society International Exchanges grant (IEC \NSFC\191600) and the National Natural Science Foundation of China (32011530168 to M.L. and L.-N.L.), the Royal Society (URF\R\180030, RGF\EA\181061, and RGF\EA\180233 to L.-N.L.), the Biotechnology and Biological Sciences Research Council Grant (BB/R003890/1 and BB/V009729/1 to L.-N.L.). This work was partially supported by Platform Project for Supporting Drug Discovery and Life Science Research [Basis for Supporting Innovative Drug Discovery and Life Science Research (BINDS)] from AMED under grant numbers JP21am0101082 (to M.S.) and JP21am0101107 (to T.T.), and by JSPS/MEXT KAKENHI (JP19H03162 to A.Y.), RIKEN Pioneering Projects “Biology of Intracellular Environments” (to M.S.) and RIKEN BDR Structural Cell Biology Project (to M.S.). L.B. was supported by a Liverpool-Riken International PhD Studentship.

## Author contributions

M.S., M.L., and L.-N.L. conceived the study. T.T., D.P.C., M.L., and L.-N.L. designed the experiments. P.C., L.B., A.Y., B.M.C., T.N., B.Z., T.T., and D.P.C. performed the experiments. P.C., L.B., A.Y., B.M.C., T.N., B.Z., T.T., D.P.C., M.L., and L.-N.L. analyzed the results. P.C., L.B., A.Y., M.L., and L.-N.L. generated structural models. P.C., L.B., M.L., and L.-N.L. wrote the paper with contributions from all other authors.

## Competing interests

The authors declare no competing interests.

## Additional information

**Supplementary information** The online version contains supplementary material available at <https://doi.org/10.1038/s41467-022-29563-3>.

**Correspondence** and requests for materials should be addressed to Mikako Shirouzu, Mei Li or Lu-Ning Liu.

**Peer review information** *Nature Communications* thanks the anonymous, reviewer(s) for their contribution to the peer review of this work.

**Reprints and permission information** is available at <http://www.nature.com/reprints>

**Publisher's note** Springer Nature remains neutral with regard to jurisdictional claims in published maps and institutional affiliations.



**Open Access** This article is licensed under a Creative Commons Attribution 4.0 International License, which permits use, sharing, adaptation, distribution and reproduction in any medium or format, as long as you give appropriate credit to the original author(s) and the source, provide a link to the Creative Commons license, and indicate if changes were made. The images or other third party material in this article are included in the article's Creative Commons license, unless indicated otherwise in a credit line to the material. If material is not included in the article's Creative Commons license and your intended use is not permitted by statutory regulation or exceeds the permitted use, you will need to obtain permission directly from the copyright holder. To view a copy of this license, visit <http://creativecommons.org/licenses/by/4.0/>.

© The Author(s) 2022